JOURNAL OF PROPULSION AND POWER
Vol. 33, No. 6, November–December 2017

Flow Characterization of a Hypersonic Expansion Tube Facility for Supersonic Combustion Studies

Yasin M. Abul-Huda* and Mirko Gamba†
The University of Michigan, Ann Arbor, Michigan 48104

DOI: 10.2514/1.B36543

A hypersonic expansion tube facility was designed and constructed to primarily study supersonic combustion phenomena. This paper provides an overview of the range of conditions the facility is capable of generating along with a discussion on how well a number of parameters required to accurately replicate conditions for supersonic combustion are achievable. A series of experiments using three low-to-mid enthalpy conditions were used to characterize and assess the extent of impact that flow-nonidealities have on the final test gas properties. Aspects such as shot-to-shot repeatability, temporal and spatial test gas uniformity, boundary-layer properties, and the presence of flow disturbances are analyzed. The shot-to-shot variation in the measured shock speeds corresponded to acceptable bulk variations of the aerothermodynamic properties of the test gas flow. Temporally, both the static and total pressures increased over the test gas slug, offsetting each other in a manner that kept the inferred test gas Mach number constant. Spatially, it was found that the core flow size increases with increasing test gas pressure and to a first order can be approximated to span 2/3 of the pipe diameter for the range of conditions considered. The presence of test gas flow disturbances was found to be negligible as the conditions studied exhibited a weak frequency focusing effect. Lastly, an improved method of acquiring high signal-to-noise ratio static pressure measurements in such impulse facilities was demonstrated to reduce measurement noise by as much as 70%.

Nomenclature

a	=	speed of sound
a_d	=	secondary diaphragm acceleration
H_0	=	total enthalpy
h	=	enthalpy
L	=	length scale
L_{ts}	=	test gas slug length
M	=	Mach number
q	=	dynamic pressure
P	=	static pressure
P_a	=	temporal mean of test gas pressure during useful test time
P_t	=	pitot pressure
R	=	tube inner radius (7.2 cm)
$\mathcal{R}$	=	specific gas constant
Re	=	Reynolds number
r	=	radial coordinate direction originating from centerline
T	=	temperature
T_{aw}	=	adiabatic wall temperature
T_c	=	combustor entry temperature
T_f	=	ambient freestream temperature
T_w	=	wall temperature
t	=	time
$\tilde{t}$	=	ratio between available test time and establishment time
$\hat{t}$	=	ratio of elapsed time by the total useful test time
t_{ts}	=	test time
U	=	flow speed in streamwise direction
x	=	streamwise coordinate direction
δ	=	boundary-layer thickness
δ_d	=	secondary diaphragm thickness
γ	=	ratio of specific heats
ϕ	=	equivalence ratio
ρ	=	density
ρ_d	=	secondary diaphragm density
θ	=	characteristic temperature
τ_{ig}	=	ignition delay time

Presented as Paper 2015-1785 at the 53rd Aerospace Sciences Meeting, Kissimmee, FL, 5–9 January 2015; received 14 November 2016; revision received 10 February 2017; accepted for publication 19 February 2017; published online 15 May 2017.

*Graduate Research Assistant, Department of Aerospace Engineering; yasinma@umich.edu. Student Member AIAA.

†Assistant Professor, Department of Aerospace Engineering; mirkog@umich.edu. Member AIAA.

I. Introduction

FOR over 50 years, the development of scramjet technology has relied heavily on ground test facilities for design validation purposes. The underlying physics present in the supersonic/hypersonic flow regime is of a highly complex and coupled nature in which the effects of chemistry, nonequilibrium, turbulence, and compressibility each play an important role in governing the behavior of the fluid flow. Understanding each of these aspects individually and how they couple with one another is of key importance when designing future hypersonic aircraft.

Recently, there have been efforts to advance hypersonic flight technology through a number of flight experimentations using instrumented ballistic reentry vehicles to study several hypersonic flow phenomena. Collaborative efforts such as the HIFiRE and HyShot programs have successfully tested subscale scramjet vehicles in true-flight environments [1–4]. Some of the objectives of these flights were to test the performance of dual-mode to scramjet-mode transition, demonstrate Mach flight numbers ranging between 6 and 8, and the use of hydrocarbon fuels, laminar to turbulent boundary-layer transition, steady and unsteady combustion, and more. In spite of these successful missions, the use of ground test facilities remains the workhorse for the advancement of hypersonic technology due to its relatively simpler and lower cost of operation [5,6].

Impulse facilities such as shock tunnels, expansion tubes, and expansion tunnels allow the replication of high-Mach number and high-enthalpy flows. A number of these facilities have been constructed in the effort of studying supersonic flows over several applications, such as those of reentry vehicles or scramjet combustors. Several of these facilities include the Large Energy National Shock Tunnel Facilities at CUBRC [7]; NASA's HYPULSE facility at GASL [8,9]; the X-series and T4 facilities at the University of Queensland [10–12]; the free-piston shock tunnel T5 [13] and the hypervelocity expansion tube (HET) at GALCIT [14]; the JX-1 in Tohoku, Japan [15]; the HIEST facility in Kakuda, Japan [16,17]; and the HEG facility at the German Aerospace Center (DLR) [18,19].

More recently at the University of Michigan, we have designed and constructed a new expansion tube facility to access aerothermal flow

conditions relevant to scramjet mixing and combustion studies. We refer to this facility as the Michigan Hypersonic Expansion Tube Facility (MHExT). In particular, the system was designed to generate aerothermal flow conditions representative of flight Mach numbers ranging between 4 and 11. Ideally, an expansion tube offers the potential of accessing a wide range of aerothermal conditions by leveraging two unsteady wave processes. However, the advantages of using an expansion tube over other facilities come at a cost, as they are inherently limited by short test time durations and limited core flow sizes. Furthermore, nonideal effects such as flow disturbances and boundary-layer growth that cause spatial and temporal nonuniformity can have significant effects on the final test gas flow properties [20–23]. A sufficient understanding of the generated test flow properties and characteristics is required to accurately isolate facility-induced effects on processes being studied such as mixing, ignition, and flame-holding. Therefore, the present study provides the foundational groundwork necessary for future supersonic mixing and combustion experiments.

The present work discusses the development of the facility, an analysis on the use of the facility for supersonic combustion studies, the characterization of a few relevant flows that it generates, as well as a few practical considerations related to proper test-model instrumentation. In this study, we examine a total of three flow conditions generated by MHExT, where two were specifically designed to represent the combustor entry conditions for the recent HIFiRE II project. We investigate the aerothermal properties and evaluate the impact of expansion tube nonidealities on the generated flows. In particular, a series of experiments were carried out to analyze shot-to-shot repeatability, temporal and spatial test gas uniformity, boundary-layer properties, and the presence of flow disturbances. Furthermore, we define properties such as the core flow size and useful test time.

The analyses and experiments of this work treat the expansion tube as a direct-connect facility in the sense that the generated test gas flows have an aerothermodynamic state representative of combustor entry conditions. It is equivalent to isolating the combustor section from the flow processes associated with the forebody and inlet of an actual vehicle. Although this provides a platform for well-controlled and fundamental studies of supersonic combustion phenomena, it neglects any coupling between the combustor and inlet flow processes. Because distortions of the flow profile and boundary layer within scramjet inlets are believed to affect the subsequent mixing and combustion processes [24–26], a complete system-level evaluation of performance requires integration of the combustor with the aircraft.

II. Background

A. Expansion Tube Theory

The operation of an expansion tube was originally proposed and analyzed theoretically by Trimpi [27]. It is capable of accessing a wide range of aerothermal conditions with considerable gains in both stagnation enthalpy and pressure. The underlying principle relies on processing the test gas through a series of unsteady waves to generate a desired high-enthalpy supersonic/hypersonic aerothermal test gas flow. The generated test gas may be designed to replicate a wide range of flow regimes, such as those found in supersonic combustors or reentry vehicles.

An expansion tube comprises three main parts, referred to as the driver, driven, and expansion sections. Before each test run, the sections are separated by diaphragms and filled with various gases to predetermined pressures. The driven section is filled with the test gas, which can be any mixture of interest. The pressure and sound speed ratios across each diaphragm before rupturing determine the strengths of the generated waves and, therefore, the final test gas properties. What differentiates an expansion tube from other impulse facilities such as reflected shock tunnels is the process used to reach the final aerothermodynamic state of the test gas. In particular, after being compressed by the incident shock wave generated by the rupture of the primary diaphragm, the test gas is further processed by an unsteady expansion wave generated by the rupture of the secondary diaphragm. This results in further acceleration of the test gas to higher Mach numbers as well as an increase in its total enthalpy and pressure.

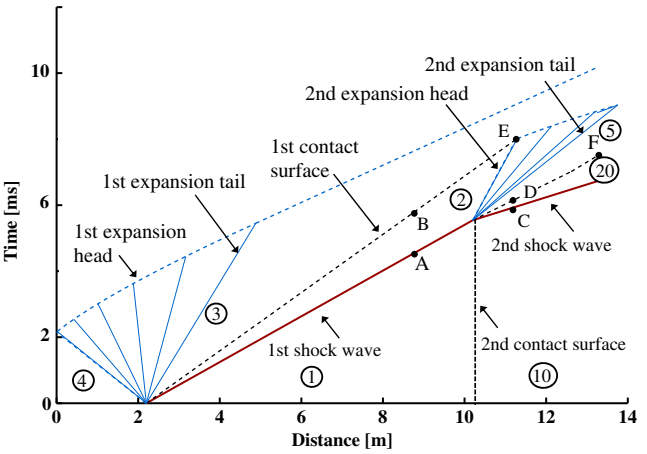

Fig. 1 Computed space–time diagram of the wave trajectories during the operation of MHExT for flow condition B.

An example of the computed wave processes that are present during the operation of an expansion tube is shown as a space–time diagram in Fig. 1. The x–t diagram corresponds to flow condition B, and the initial fill conditions are detailed in Table 1. The labeling of the various states of gas follows the convention of Trimpi [27]. The diagram shows how a second pair of waves is formed at the secondary diaphragm upon arrival of the incident shock wave. The second shock wave continues propagating through the expansion gas (region ⑩), whereas the expansion wave processes the test gas to its final state (region ⑤). Because the induced bulk motion of the test gas after the incident shock wave (region ②) is usually supersonic (for high-enthalpy operation), the secondary expansion wave is swept downstream as shown in the figure. The test time begins with the arrival of the second contact surface (labeled F) and is limited by the arrival of either of the following three waves: 1) the tail of the second expansion wave; 2) the reflection of the second expansion wave head off the first contact surface; or 3) the reflection of the first expansion wave head off the driver end wall.

There are a number of advantages that expansion tubes have over other impulse facilities such as reflected shock tunnels. First, expansion tubes can be operated over a wide range of conditions by only varying the compositions and fill pressures of each section. This eliminates the requirement of replacing a nozzle to alter the test gas Mach number. Second, the process never involves stagnating the test gas, but rather does work on the test gas as it is moving through the secondary unsteady expansion wave. For a wide range of conditions relevant to supersonic combustion, the flows will have negligible amounts of dissociation and thermochemical nonequilibrium, and are thus more representative of the desired flight conditions being replicated. This is of particular importance in high-speed combustion studies as the chemical composition of the test gas is a significant parameter that must be replicated accurately [6,28,29]. Furthermore, higher stagnation pressures and temperatures are achieved in the test gas with an expansion tube for the same initial driver fill pressure and gas sound speed as a shock tunnel. This is a further benefit of the unsteady expansion processes.

Nevertheless, the advantages of using an expansion tube do come at a cost as they are inherently limited by short test time durations and limited core flow sizes. Furthermore, nonideal effects such as flow disturbances and boundary-layer growth that cause spatial and temporal nonuniformity can have significant effects on the final test gas flow properties. We evaluate these effects and limitations in our facility through a set of experiments that include fast-response pitot and static pressure measurements as well as high-speed schlieren images of the development of the flow around a simple geometry.

Table 1 Summary of the MHExT performance based on a statistical analysis of the shot-to-shot variability

Condition	A	B	C
Initial setup			
Composition [driver-driven expansion]	[He Air He]	[He Air He]	[Air Ar He]
Driver fill pressure, kPa	1896	1724	586
Driven fill pressure, torr	74.3	45.4	82.8
Expansion fill pressure, torr	148.2	36.6	50.2
Test gas properties			
Nominal flight Mach number	6	8	NA
Primary shock speed[a], m/s	$1351 \pm 0.5\%$	$1442 \pm 0.6\%$	$696 \pm 0.3\%$
Secondary shock speed[a], m/s	$2160 \pm 0.2\%$	$2585 \pm 0.5\%$	$1562 \pm 0.3\%$
Mach number[a]	$2.07 \pm 0.6\%$	$2.75 \pm 0.9\%$	$1.73 \pm 3.3\%$
Mach number[b]	$2.05 \pm 0.5\%$	$2.76 \pm 0.6\%$	$1.76 \pm 0.6\%$
Static pressure (test section)[a], kPa	$122.4 \pm 0.9\%$	$49.1 \pm 0.9\%$	$25.6 \pm 0.5\%$
Static pressure (tube wall)[a]⑳, kPa	$107.6 \pm 0.4\%$	$39.1 \pm 0.8\%$	$18.3 \pm 0.6\%$
Static pressure[b], kPa	$106.1 \pm 0.4\%$	$38.0 \pm 0.9\%$	$18.0 \pm 0.7\%$
Test time (total)[a], μs	$950 \pm 5.0\%$	$920 \pm 8.8\%$	$5540 \pm 1.8\%$
Test time (useful)[a], μs	$550 \pm 7.9\%$	$690 \pm 19\%$	$4570 \pm 13\%$
Test time (Mirels)[c], μs	880	940	5450
Stagnation enthalpy[b], MJ/kg	$1.92 \pm 0.3\%$	$2.37 \pm 0.6\%$	$0.44 \pm 0.7\%$
Static temperature[b], K	$980 \pm 0.5\%$	$910 \pm 0.7\%$	$420 \pm 0.3\%$
Velocity[b], m/s	$1259 \pm 0.3\%$	$1637 \pm 0.7\%$	$673 \pm 0.7\%$
Reynolds number[b]	8×10^7	1×10^8	7×10^5
Secondary diaphragm accel.[b], m/s^2	4×10^8	3×10^8	7×10^7

Aerothermodynamic properties pertain to the test gas (region 5) unless otherwise noted.
[a]Measured quantity.
[b]Semitheoretical quantity.
[c]Theoretical quantity.

B. Design and Operation Overview of MHExT

The MHExT facility is composed of a 14-m-long stainless steel pipe, comprising three main sections each capable of withstanding pressures of up to 80 bar. A schematic of the completely assembled facility is shown in Fig. 2. The driver, driven, and expansion sections have a honed and polished internal diameter of $2R = 144$ mm and are 2.9 m, 8 m, 3 m long, respectively. The tube is composed of seven subsections such that the test time of any desired condition can be optimized by leveraging its modular design. The entire tube rests on rollers to allow diaphragm changing as well as an easier way to interchange the subsections. The dump tank and driver section rest on their own independent carriage structures. This allows for complete detachment in order to more easily access the interior of the tube for routine inspections and cleaning.

The driver and driven sections are separated by the primary diaphragm that employs a double-diaphragm design. This configuration uses an intermediate section (buffer) to better control rupture initiation of the diaphragm, leading to increased repeatability of test conditions between individual runs. This is accomplished by isolating the buffer between two individual diaphragms (usually one or more scored polycarbonate sheets) and filling it with an intermediate pressure relative to that of the driver and driven sections. Upon evacuating the buffer, the upstream diaphragm rapidly ruptures due to the increase in pressure differential across it and is shortly followed by the rupture of the downstream diaphragm. These sheets are typically prescored with a cross pattern such that, upon rupture, the diaphragms open into four petals that fold and conform to the interior walls of the buffer section that has a square inner cross section to facilitate the complete opening of the diaphragm petals. This design serves to minimize flow disturbances originating from the primary diaphragm rupturing process.

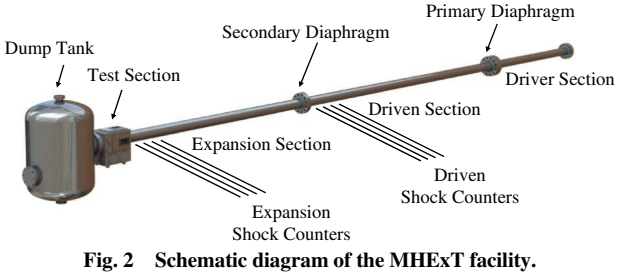

Fig. 2 Schematic diagram of the MHExT facility.

The driven and expansion sections are separated by a thin polyester film, which is 2 μm in thickness. Previous studies [30] have shown that the secondary diaphragm thickness had no measurable effect on the final test gas properties for conditions similar to what are considered here. However, using thinner membranes can help reduce measurement noise of the test gas static pressure. The parameter used to compare our study to others is the secondary diaphragm acceleration [31], which is a measure of the extent in which the secondary diaphragm influences the pressure distribution of the flow. The diaphragm acceleration can be approximated to be

$$a_d = \frac{P_6 - P_{10}}{\rho_d \delta_d} \tag{1}$$

where ρ_d and δ_d are the diaphragm density and thickness, respectively. P_6 is the post-reflected-shock pressure of the gas initially in state ②. The secondary diaphragm accelerations for the three flow conditions of this study are tabulated in Table 1. Furukawa et al. [31] showed that the use of thinner secondary diaphragms increases the diaphragm acceleration and therefore minimizes the formation of a reflected shock wave. This in turn minimizes any alteration of the test gas due to the diaphragm rupturing process. In particular, they have shown that by using polyester film diaphragms 3 μm in thickness, the strength of the reflected wave can be reduced to that of a Mach wave.

A test section and dump tank are located at the end of the expansion section and are mated with one another through a rubber expansion joint. This allows the dump tank to recoil relative to the test section during each test run, while maintaining the required sealing. The test section is a stainless steel rectangular chamber 45.7 cm × 48.3 cm × 34.3 cm in size. Three quartz windows are used for optical access through the test section in order to carry out nonintrusive diagnostic techniques. Several feed-through ports as well as access panels are distributed along the sides of the test section for additional instrumentation. The test section is independently anchored to the laboratory's floor and it is joined to the expansion section through dynamic o-rings to allow for relative movement of the tube while providing vacuum-tight sealing. The dump tank is approximately

1 m^3 in volume and was designed to be sufficiently large to maintain a nearly constant dump tank pressure during the usable test time as well as maintain a subatmospheric pressure within the facility at the end of each test run.

Data acquisition and control of the system is carried out using a computer-based system. The system is composed of a National Instrument 9-Slot PXIe-1078 Chassis, which houses two NI PXI-6133 DAQs, one NI PXI-2521 relay module, and a PXIe-PCIe8381 controller. The system is instrumented with analog and digital input/output modules operated by a Labview program and interfaced with a multitrigger digital delay generator to provide timing and synchronization to external instrumentation, such as solenoid valves, MKS Baratron vacuum transducers, PCB sensors, lasers, and cameras. Data acquisition of pressure transducers, for example, is carried out at a rate of 2 MHz.

Over 70 side-wall ports and plugs are located along the tube to provide access for instrumentation, such as pressure transducers, and optical access for nonintrusive laser diagnostic measurements. To measure the speed of the primary and secondary shock waves, eight PCB Piezotronics 113B27 pressure sensors are used as time-of-arrival shock counters. Four of the sensors are mounted into ports spaced 30.5 cm apart located just upstream of the secondary diaphragm. A similar four-sensor set up is used just upstream of the test section to measure the secondary shock speed. The shock speeds U_{s1} and U_{s2} are computed from the time of flight between sensors, and are then used to determine the test gas conditions using a solver (described in the Appendix) that models expansion tubes and includes equilibrium temperature-dependent properties constructed after the analysis of Trimpi [27]. Before operation, each section of the tube is evacuated with its own designated vacuum pump. During the fill and evacuation processes, the pressures in the driven and expansion sections are monitored using Baratron 627D temperature-regulated capacitance manometers.

III. Requirements for Supersonic Combustion Studies

In the following section we discuss a number of important aspects regarding the use of an expansion tube facility for scramjet combustion studies. We assess how well the MHExT facility performs by satisfying the requirements needed to generate flows that properly replicate conditions for supersonic combustion studies. Unless otherwise stated, the combustor entry conditions were computed using a generic two-shock inlet, shown schematically by the inset of Fig. 3, to process ambient air over the course of a predetermined flight envelope. The flight envelopes follow constant dynamic pressure trajectories of either $q = 50$ kPa or $q = 100$ kPa, which represent the limiting operational bounds for hypersonic aircraft [28]. The solver used to compute the postshock properties assumes that the gas is in equilibrium and considers real gas effects. The inlet is chosen to have an inward turning angle of 20 deg so as to keep the combustor entry temperature, $T_c < 1700$ K [28], at a flight Mach number of 10. This, however, results in a fairly low combustor entry temperature of approximately 700 K at a flight Mach number of 6. The implication on our analysis is a lower-than-desired flow enthalpy at the early stages of the flight envelope. Nevertheless, because the inlet compression ratio remains a function of flight Mach number, the analysis has a certain degree of consistency and provides valuable insight, while not impacting the conclusions.

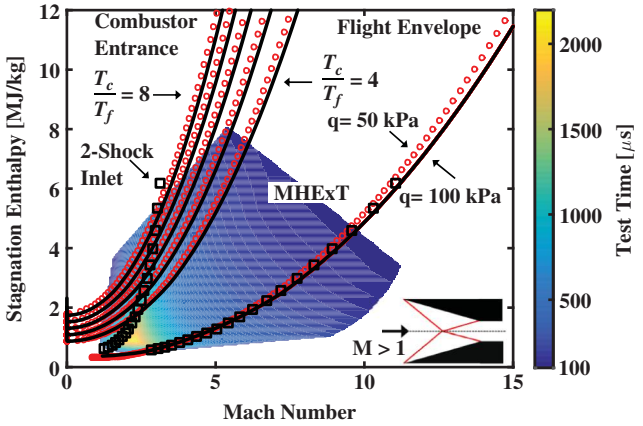

Fig. 3 Energy requirements to properly replicate conditions for supersonic flight superimposed over the range of achievable conditions with MHExT.

A. Energy Requirements

Our first assessment is on the capability of the facility in generating the energy required to properly replicate conditions for hypersonic flight. We use two methods to compute the combustor entry conditions for a hypersonic vehicle flying along a constant dynamic pressure envelope. The analysis of the first method (outlined in [28]) is limited in scope, as it assumes a constant compression ratio T_c/T_f across the inlet for a range of flight Mach numbers. In reality, this ratio is a function of flight Mach number for a fixed inlet design/geometry. Therefore, we extend our analysis through a second method that uses a generic two-shock inlet.

The results of both methods are shown in Fig. 3. The circle symbols ($q = 50$ kPa) and solid lines ($q = 100$ kPa) correspond to the first method. The curves on the right-hand side of the figure indicate the expected total flow enthalpy as a function of flight Mach number. The curves on the left-hand side of the figure show the corresponding combustor entry Mach number following the inlet compression process, which reduces the Mach number while maintaining a constant total enthalpy. The various circle and solid curves pertain to varying degrees of compression across the inlet (constant T_c/T_f value for each curve). The square symbols correspond to the second method for a constant $q = 50$ kPa flight envelope. As expected, with the two-shock inlet we observe an increasing inlet compression ratio (T_c/T_f) with increasing flight Mach number. We also observe that the energy requirements increase rapidly with flight Mach number where approximately 5 MJ/kg is required for a flight Mach number of 10.

Superimposed on Fig. 3 is a color contour plot of the range of achievable test gas conditions with the MHExT facility, which should be compared with the combustor entry condition curves. The contour indicates the achievable test times for varying flow Mach numbers and stagnation enthalpies. The solution of all possible achievable test gas aerothermodynamic states was obtained by using the expansion tube solver outlined in the Appendix. The solution was specific to helium, air, and helium as the driver, driven, and expansion gases, respectively. The fill pressures spanned the capability of the facility while being limited by practical considerations, and were as follows: $13 < P_4$ [kPa] < 11750; $10 < P_1$ [torr] < 1000; $1 < P_{10}$ [torr] < 150. Because MHExT has a modular design, the color contour plot shown indicates the test times achievable with only one of its three configurations, which is intended to maximize test times for conditions representative of flight Mach numbers ranging between 6 and 8.

Based on these results, we can see that the MHExT facility is capable of generating a wide range of test gas conditions that satisfy the energy requirements of hypersonic flight. The test times range from the order of hundreds of microseconds to several milliseconds.

B. Combustion Scaling

Ground test facilities are typically incapable of testing full-scale models. Therefore, we rely on scaling laws to accurately replicate governing parameters that control processes such as mixing, ignition delay, and reaction time. Combustion scaling laws allow us to understand how to properly design experiments, interpret ground test data, and relate the results to actual full-scale flight conditions. By manipulating several flow properties, such as pressure, temperature, speed, and gas composition, we can scale several important flow parameters. For the purpose of supersonic combustion studies, some of these parameters include the flow Mach number, Reynolds number, Damköhler number, and Stanton number.

An analysis outlined by [32] is used to relate several flow properties to parameters. We arrive at a slightly different result with

the following procedure. From their definitions, M and Re depend on flow properties as,

$$M \sim \frac{U}{\sqrt{T}} \tag{2}$$

$$Re \sim \frac{\rho L M}{T^{\beta}} \tag{3}$$

The value for β arises from combining the temperature dependence of viscosity of the gas, which is sufficiently approximated by $\mu \sim T^{k}$, where $k = 0.65$ for air, with that of the speed of sound in the definition of Mach number. The combination leads to $\beta = k - 0.5 = 0.15$. Although the value of β depends on the expected dependence of viscosity on temperature (i.e., on k), in general, the temperature dependence of Re is expected to be fairly weak because k is nearly 0.5. The two nondimensional quantities describe the fluid dynamic properties of the process. To describe the relative importance of the combustion-related properties, we can use a Damköhler number, which is generally defined as the ratio of a flow to chemical time scale. Here, we define an effective Damköhler number (Da_e) to be proportional to the ratio of a flow through time and ignition delay time. This quantity depends on aerothermodynamic properties as

$$Da_e \sim \frac{L}{U\tau_{\text{ig}}} \sim \frac{\rho L U T^{(3/2)+\beta} e^{-\theta/T}}{T^{(1/2)+\beta} A U^2} \sim Re \frac{T^{(3/2)+\beta} e^{-\theta/T}}{A U^2} \tag{4}$$

where the value of ignition delay τ_{ig} is based on an Arrhenius form given by

$$\tau_{\text{ig}} = A P^{\alpha} e^{\theta/T} \tag{5}$$

and it is assumed that ignition delay is controlled by binary reactions. Equation (4) is the effective flow Damköhler number cast in terms of its explicit dependence on Reynolds number, temperature, and flow speed. The significance of this expression is that it shows how the chemical requirements for a binary reaction can be satisfied by directly replicating several flow parameters. By simultaneously replicating the flow speed, temperature, and Reynolds number of an actual system, one can replicate the Damköhler number. However, in most cases, it is challenging, if not impossible, to replicate the intended model length scale L. In this case, the Reynolds number can be replicated through its implicit dependence on density to compensate for limitations in model length scales, thus preserving the required value of Da_e.

Table 2 shows the values of the coefficients in the Arrhenius equation for hydrogen and Jet-A/JP-8 combustion with air. The table also shows the range in which the values are valid. The values for hydrogen are based on the work of Pergament [33], whereas the values for Jet-A/JP-8 were computed through a linear regression analysis using CHEMKIN and the mechanism by Wang et al. [34] and agree well with values available in the literature [35–37]. The linear fit for the parameters of Eq. (5) was done over two temperature ranges because the ignition characteristics were observed to change at approximately 2000 K. Moreover, the ignition delay is expected to increase significantly for temperatures below the specified ranges. This results from a significant increase in the activation energy required to initiate reactions. This is an important aspect to consider because a portion of our analysis, during the early portions of the flight envelope, involves initial mixture temperatures that are below the specified ranges. However, this effect does not alter our conclusions in the assessment of the facility. Lastly, the ignition delay times of Jet-A and JP-8 are identical, as the small amount of additives present in JP-8 does not seem to significantly impact the ignition characteristics.

Table 2 Coefficients for the Arrhenius equation where combustion is with air

	A, s	α	θ, K	P, kPa	T, K	ϕ
Hydrogen	8×10^{-9}	−1	9600	20–500	1000–3000	0.4–2
Jet-A/JP8	1.1×10^{-9}	−1	16,700	50–100	1200–2000	1
Jet-A/JP-8	3.3×10^{-8}	−1	10,100	50–100	2000–2500	1

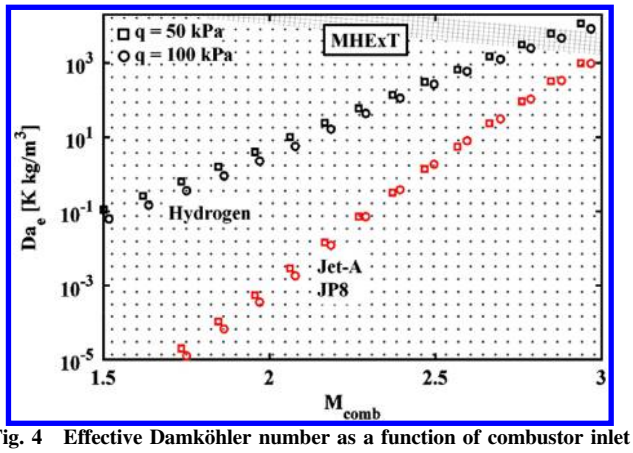

Fig. 4 Effective Damköhler number as a function of combustor inlet Mach number. Regions with a grid and dot pattern correspond to accessible conditions with MHExT.

We assess how well the MHExT facility is capable of generating flows that have equivalent values of Da_e to those of a hypersonic vehicle flying between flight Mach numbers of approximately 5 and 10 along constant dynamic pressure trajectories. Following a similar procedure used to generate the contour plot of Fig. 3, Da_e was computed from the range of aerothermodynamic properties that can be generated by MHExT. The length scale used for all of the calculations was equivalent to the inner diameter of the tube. However, because Da_e depends linearly on a length scale, the solution can be scaled accordingly to accommodate different-scale systems.

The results are presented in Fig. 4, where Da_e is given as a function of combustor entry Mach number. The regions with a grid and dot pattern correspond to the range of conditions achievable by the MHExT facility. The combined dot and grid regions correspond to hydrogen–air combustion, whereas the dot-patterned region alone corresponds to Jet-A/JP-8-air combustion. The square and circle symbols correspond to flight envelopes along constant $q = 50$ kPa and $q = 100$ kPa trajectories, respectively, assuming a hypothetical vehicle with the same generic two-shock inlet discussed previously. The results show that, for a vehicle with a characteristic length scale equivalent to the tube inner diameter, the MHExT facility is capable of replicating Da_e for flight Mach numbers up to approximately 9 and 10 for hydrogen–air and Jet-A/JP-8-air combustion, respectively.

C. Flow Establishment Time

The flow establishment process around a test model will further reduce the inherently short test times of impulse facilities. The complex regions of flow dominated by separation, viscous interaction, or shocks rely on several mechanisms, such as acoustic propagation and molecular diffusion, to adjust local properties to their test gas steady-state values. As a result, the flow establishment process inevitably consumes a portion of the available test time. In order for the useful test time to exceed the required flow establishment time, the test gas (state ⑤) slug length ($L_{\text{ts}} = U_5 t_{\text{ts}}$), which is the distance the slug of test gas travels over the test time, must satisfy

$$L_{\text{ts}} > K L_e \tag{6}$$

where K is a factor that depends on the flow process of interest, and is greater than or equal to one. Empirically correlated values of K for various flow processes are available in the literature and are provided in Table 3 for convenience [38–42]. L_e is a characteristic length scale equivalent to the size of a relevant fluid or geometric region and is equivalent to

Table 3 Summary of characteristic lengths L_e used in this study and the corresponding values of K taken from literature data

Flow process	Laminar boundary layer	Turbulent boundary layer	Bluff body separated flow	Shock-induced shear layer	Separated shock
L_e, mm	$R\tan[(\pi/2) - \sin^{-1}(1/M_5)]$[a]		30	15	$1.1d(\rho_5/\rho_{5s})$
K	3.33	2	30	1	$((\rho_{5s}/\rho_5) - 1)\ln(1 - (L'_e/L_e))^{-1}$
Reference	[38]	[38]	[39,40]	[39,42]	[41,43]

[a]Expression applies to both laminar and turbulent boundary layers.

$$L_e = Ut_e \tag{7}$$

where t_e is the establishment time and U is a characteristic flow speed and can be taken to be equivalent to U_5 or a_5, depending on the flow process.

Before we can assess how well the MHExT facility can satisfy the criterion of Eq. (6), we first explain our reasoning in choosing the values of L_e. Table 3 shows the characteristic length scales L_e chosen in this study for five relevant unit flow processes. For a laminar and turbulent boundary layer on a flat plate, L_e is equal to the length of the expansion cone emanating from the exit of the expansion tube. This length is then a function of M_5 and represents the approximate length of the boundary layer that can be contained inside of the useful core flow. In the case where a separated flow is present in the aft region of a bluff body, a length of 30 mm was chosen as an arbitrary yet typical test-model diameter. The characteristic length for the case of a shock-induced shear layer was chosen based on the size of boundary-layer separation observed upstream of a transverse jet in supersonic crossflow [44]. Separation results from the adverse pressure gradient induced by the bow shock that wraps around the jet. The presence of this region of relatively stagnant gas forms a shear layer with the supersonic free stream. Schlieren images were used to measure the size of a recirculation region in the case of a jet with a momentum flux ratio of 5.0 and was found to be approximately 15 mm in length. Lastly, in the case of a separated shock that forms around a blunt body, the characteristic length scale L_e is equivalent to the asymptotic value of the shock stand-off distance, and it is given by the empirical correlation of Farris and Russell [43]. ρ_{5s} is the fluid density behind a normal shock at state ⑤ conditions. In our study, the length d, which is the diameter of the geometric body, was taken to be 30 mm because it is a practical and representative size for a test model. Lastly, the bow shock was considered to be fully established when the value of L'_e was equivalent to 95% of L_e.

The establishment times for the five cases were computed for a range of combustor entry conditions using Eq. (7), where $U = U_5$ for all cases except for the shock-induced shear layer process, in which case $U = a_5$. This is because the underlying establishment process relies on acoustic propagation to generate the dimensions and flow topology within the separated region. The value of a_5 is computed at an intermediate temperature such as the Eckert reference temperature. The results are shown in Fig. 5, where the solid curve corresponds to the left axis and represents the total enthalpy for a flight Mach number range between approximately 5 and 10. The symbols for different flow processes correspond to the right axis. $\tilde{t}$ is the ratio between the available test time and the required establishment time of a unit flow process for an equivalent flow condition. The test time duration capable of being generated with the facility is extracted from the contour plot of Fig. 3, along the "two-shock inlet" curve.

The results of Fig. 5 show that the facility is capable of generating values of $\tilde{t}$ greater than unity for all flow processes over the range of conditions considered. However, care needs to be taken for studies involving bluff body separated flows, as the values of $\tilde{t}$ lie between 1.3 and 1.8. This requires data acquisition to be limited to the very end of the test gas slug. All other flow processes have values of $\tilde{t} > 2.3$ for the range of conditions considered. This implies that more than half of the test gas slug will convect over the test model under fully established steady conditions. It is also important to note that the correlated values of K were developed in a shock tube environment where the flow was impulsively started after the passage of a shock. An expansion tube differs in that after the passage of the secondary shock, the arrival of the test gas flow is preceded by the expansion gas. This effectively reduces the flow establishment times of expansion tube flows to as much as 2/3 of that predicted by the shock tube experiments [32].

Typically, the flow over a test model will involve a combination of the unit flow processes. Therefore, the total flow establishment time can be conservatively approximated to be a linear combination of all of the individual relevant unit flow processes. The total establishment time t_{total} would then be

$$t_{\text{total}} = \sum_i C_i t_{e_i} \tag{8}$$

where $0 < C_i \leq 1$. Values of C_i would be very challenging to measure experimentally, and the most conservative value would be one. The reasoning behind this expression is based on the idea that the individual unit flow processes will affect one another while simultaneously adjusting to the ideally impulsively started test gas flow.

IV. Facility Characterization

A total of three conditions were designed to span a range of properties accessible by the facility while maintaining relevance to the study of supersonic combustion. The first two are referred to as conditions A and B and correspond to Mach 6 and 8 flight, respectively. These flows have aerotherodynamic properties similar to the combustor entry conditions of the hypersonic test vehicle in the recent HIFiRE Flight-2. During the test window of this experiment, the flight envelope consisted of flight Mach numbers ranging between 6 and 8.5 at a constant dynamic pressure of 86.2 kPa. Using this information, a method discussed in [28] was followed to estimate the resulting combustor entry properties defined in this study. The third condition, referred to as C, is a relatively lower-enthalpy flow with a longer test time. It is of interest to the studies of processes that do not require high static temperatures and/or require longer test times. The longer test time was achieved by increasing the ratio of sound speeds a_1/a_4, which generates a relatively weaker set of incident waves and increases the time before the second expansion head is reflected off of the first contact surface.

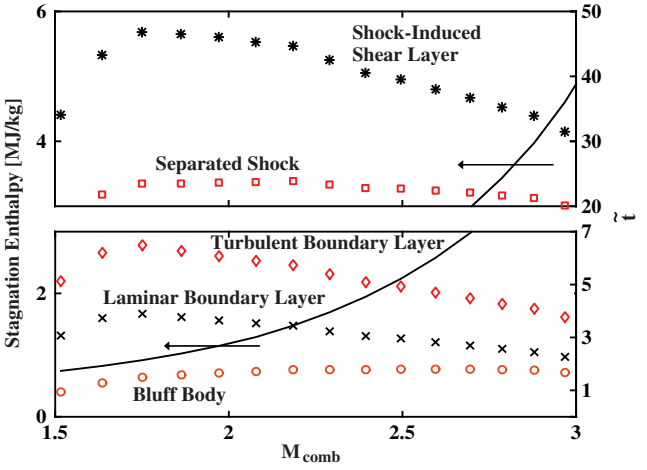

Fig. 5 Flow establishment time (symbols) and stagnation enthalpy (solid curve) over a range of combustor inlet Mach numbers.

A detailed summary of various aerothermal flow properties, such as a comparison of those that were experimentally measured and computed based on the expansion tube solver, is given in Table 1, and will be discussed further in the subsequent sections. A representative set of the experimental results for all the three conditions is presented in the paper to give the reader a sense of their characteristics.

A. Time History Measurements of Bulk Flow Properties

Because the test gas convects a considerable distance before reaching the test section, the growth of the boundary layer will cause nonuniform, axial variations in the test gas properties. According to the work of Mirels [20,21], until the limiting distance between the shock and contact surface is reached, the effects that result from boundary-layer growth are a function of both time and axial location along the tube. Because the limiting distance is not reached in any of the conditions of the present study, the measurements taking place in the test section during the test gas flow are affected by a combination of both temporal and axial variations within the test gas slug. To understand how these combined effects alter the test gas properties, pitot and static pressure measurements were simultaneously carried out to directly measure the test gas pressure and infer the flow Mach number.

The assembly shown schematically in the inset of Fig. 6a was used for pitot–static measurements in the test section just downstream of the exit of the tube. The assembly consisted of a flat plate with a sharp leading edge and was instrumented with a static and a stagnation pressure probe composed of fast response piezoelectric pressure transducers (PCB 113B21). The static pressure measurements were taken by a flush-mount surface sensor located approximately 72 mm downstream of the exit plane. The pitot pressure measurements were taken by a conical pitot tube axially co-located with the static transducer and centered on the center line of the tube. The pitot tube housed a recessed mounted piezoelectric transducer and was located 2.5 probe body diameters off the surface of the plate. The pitot–static measurements are limited both spatially and temporally due to the relatively large effective surface area of the sensing element (about 3 mm × 3 mm) and the effective response time associated with each mounted sensor, which includes a contribution due to the inherent response of the transducer and the response of the mounting cavity of the recessed mounted sensor. Because the specified rise-time of the sensors is on the order of 1 μs or less, the primary contributor is a result of the recessed mounting that may delay the response by several 10 s of microseconds.

An example of a simultaneous pitot–static pressure measurement for flow condition B is shown in Fig. 6a. P_a is the mean static pressure over the useful test time and has a value of 49.1 kPa. The portion labeled I shows an increase in both static and pitot pressures, and corresponds to the arrival of the secondary shock. The portion labeled II corresponds to the flow of the expansion gas over the sensors. Because the Mach number of region ⑳ is nearly sonic before exiting the tube with $P_{20} > P_{10}$, the gas entering the test section behaves as a sonic underexpanded jet. Thus, the sensor is effectively located within the expansion fan of the underexpanded jet. The decrease in static pressure in location II compared with location I is consistent with the expected lower pressure in the barrel shock of a sonic underexpanded jet [45,46].

Because the Mach numbers of the expansion and test gas are different while pressure and flow speed are the same, the pitot traces allow us to more accurately identify the different regions of the flow. The increase in the measured pitot pressure indicated by label III marks the arrival of the supersonic test gas. An increase in the static pressure is also observed and it results from the change in Mach angle of the expansion fan of the underexpanded jet, as the flow Mach number increases across the contact surface. The Mach angle decreases and creates a conical region of constant test gas properties (state ⑤) that envelops the sensor. This region of the flow outside of the expansion tube is referred to as the test gas core flow. The location of IV corresponds to a period of nonuniform flow over the sensors. During this time, we observe a number of coupled effects: 1) the effect of the finite thickness of the contact surface as it convects downstream [47–49]; 2) the transient process associated with the change in wave structure from the barrel shock of the initial sonic underexpanded expansion gas to the final underexpanded supersonic test gas flow; and 3) the establishment process of the test gas flow. The pitot trace in region IV is an artifact of the combination of all these transient processes in addition to the delayed response time associated with the recessed mounted sensor in the pitot tube. This can be shown by considering the acoustic time through the pitot tube cavity, which can be approximated as the postnormal shock freestream sound speed divided by the length of the pitot tube cavity. For example, the acoustic time scale of the cavity is approximately 20 μs for condition B. Based on the duration of region IV from the pitot trace of Fig. 6a, the time required for the pitot pressure to reach the test gas value is approximately 10 acoustic time scales. Following the transient flow of region IV is the uniform test gas flow labeled as V. This is the region of flow that we define as the useful test time and is specified as the region of the flow in which the pitot trace remains to within ±5% of its average value. The test time is terminated by the arrival of any of the rarefaction waves labeled VI.

The increase in both pitot and static pressure over the test gas slug is evident from the measurements. The effect that this trend has on the test gas Mach number was found by using the Rayleigh pitot tube formula to infer the flow Mach number. An average value of γ between the pre- and postnormal shock values was used because of the weak dependence on gamma within the temperature ranges being studied. Figure 6b shows the time history of the approximate flow Mach number as inferred by the simultaneous pitot–static pressure measurements of Fig. 6a for flow condition B. We postulate that the combined increase in static pressure and total pressure results in a flow with a nearly constant inferred Mach number. The increasing trend in measured pitot pressure is possibly the result of the secondary expansion wave processing a nonuniform gas in state ②, which results in an increase in total and static pressure in state ⑤. The

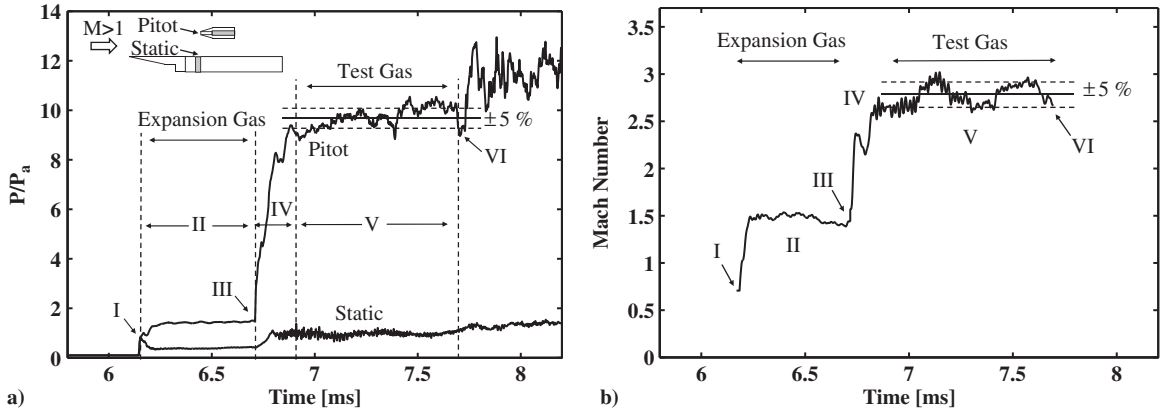

Fig. 6 a) Time history of simultaneous pitot–static pressure measurements. b) Inferred Mach number from pitot–static pressure measurements of (a). Data pertain to condition B.

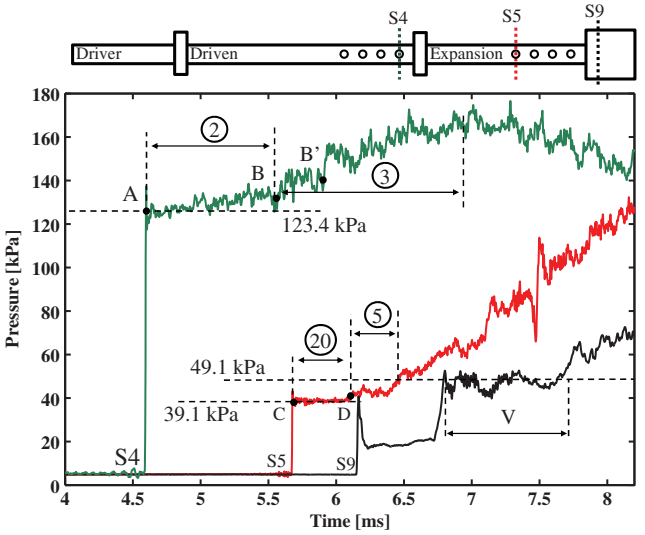

Fig. 7 Static pressure measured at three locations along the expansion tube. Data refer to flow condition B.

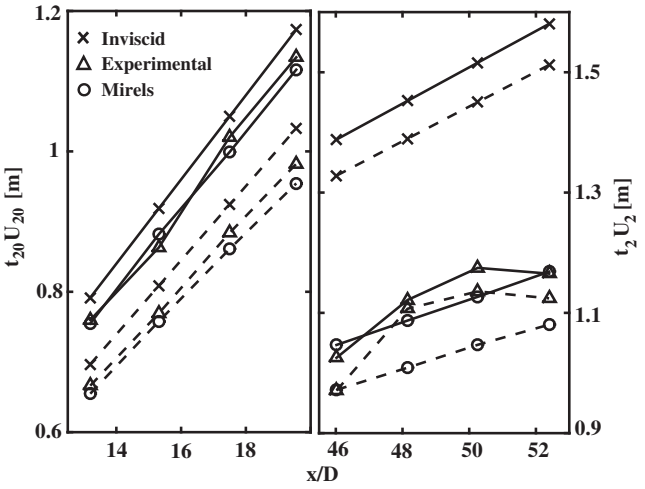

Fig. 8 Comparison of state 20 (left) and state 2 (right) nominal slug lengths using three methods (inviscid, experimental, and Mirels) for conditions A (solid) and B (dash).

nonuniformity in the shocked test gas in state ② results from the initial boundary-layer growth induced by the primary shock wave.

The temporal nonuniformity of the fluid in region ② can be seen more clearly in Fig. 7, which shows an example of the static pressure measured at three locations along the length of the tube for flow condition B. The pressure trace labeled S4 was acquired with the fourth shock counter of the driven section, which is located approximately 7.6 m downstream of the primary diaphragm (shown schematically by the inset of Fig. 7). At this fixed location, the pressure of the test gas in state ② initially has a value of ∼123 kPa (averaged over a small window after the arrival of the primary shock wave) and increases by 8% by the end of the slug. The trace labeled S5 corresponds to the static pressure measured by the first shock counter of the expansion section, which is located approximately 2 m downstream of secondary diaphragm. At this fixed location, the trace shows that there is no pressure increase during the flow of the shocked expansion gas in state ⑳. However, there is an approximate 20% increase in pressure over the test gas slug in state ⑤ before the second expansion tail arrives at this location. Finally, the trace labeled S9 was acquired in the test section approximately 3.1 m downstream of the secondary diaphragm using the same assembly described previously in Fig. 6a. At this location, the test gas pressure varies by approximately ±7% of its average value of 49.1 kPa over the slug of fluid in state ⑤.

The points labeled A through D on the traces of Fig. 7 indicate the arrival of either a compression wave or contact surface. The corresponding points are labeled in the computed x–t diagram of flow condition B, shown in Fig. 1. The x–t diagram was computed using the known fill pressures and experimentally measured shock speeds as inputs to a solver that computes the various state properties. The thermodynamic states are then used to compute the wave trajectories using the method of characteristics and unsteady shock wave theory [50]. The trajectories of the contact surfaces are corrected to incorporate the effects of viscosity through the work of Mirels [20,21]. The trends of the pressure traces were found to agree well with the computed times of arrival of the shocks and contact surfaces. For example, point A indicates the arrival of the primary shock and hence a step change in pressure. Point B indicates the arrival of the first contact surface, which is followed by a gradual increase in pressure from the gas in state ③.

The point labeled B' indicates the computed time of arrival of the first contact surface based on inviscid considerations. For this condition, the inviscid calculation underestimates the speed of the contact surface by approximately 30%. A comparison of the nominal slug lengths of gas in states ② and ⑳ is shown in Fig. 8. The results obtained using three methods are shown for both conditions A (solid) and B (dash). The time of arrival between the shock and contact surface is normalized by the corresponding nominal inviscid gas speed. The experimentally measured values are an average over three shots, and were extracted from eight shock counters along the tube's length. The arrival of the contact surface is delineated by a distinct rise and periodic fluctuation in pressure as can be seen in the S4 trace of Fig. 7. The results reveal how the inviscid calculations systematically underestimate the speed of the contact surface, which in reality accelerates. On the other hand, the solution using the model of Mirels [20,21] is in good agreement with the experimentally measured values. The remaining discrepancies may be due to a combination of the uncertainty in the measurement technique as well as the fact that the viscous correction was based on the assumption that the boundary layer was fully turbulent in states ② and ⑳, whereas theory for a transitional boundary layer may be more appropriate for these conditions.

The formation of the boundary layer acts as an aerodynamic sink that absorbs mass from the core flow. To conserve mass, the contact surface accelerates reducing its distance from the shock wave. This is observed to have a significant consequence on the test time because the reflection of the secondary expansion head off of the first contact surface (point E in Fig. 1) is usually the process that limits the test time. Effectively, the presence of boundary-layer growth in states ② and ⑳ causes points E and F in Fig. 1 to occur earlier. In turn, the accelerating first and second contact surfaces have a competing effect to reduce and increase the test time, respectively. Generally, the effect induced by the acceleration of the first contact surface outweighs the effect induced by the acceleration of the second. This results in an overall reduction in the available test time as compared with the inviscid solution. This is shown in Table 4, where a comparison of the test times for all three conditions is presented by comparing them through three methods.

The solution based on Mirels's work is obtained by treating the expansion tube as two separate shock tubes. In short, the computed test time is obtained by solving for the corrected locations of points E and F in Fig. 1. This formulation neglects any effect that the secondary expansion wave has on the boundary layer. Therefore, because the results of this analysis show a satisfactory agreement between the test time obtained experimentally and with Mirels's

Table 4 Comparison of the generated test time for three flow conditions

Condition	A	B	C
Experimental, μs	950	920	5540
Mirels, μs	880	940	5450
Inviscid, μs	1280	1120	5650

solution, we infer that the effects of the secondary expansion wave on the trajectory of the waves may be minimal.

B. Summary of Average Bulk Flow Conditions

A summary of the initial and resulting test gas bulk flow properties for each of the three selected test conditions is given in Table 1. The indicated uncertainties are based on a total of 15 runs for each condition where the only exception is the measured Mach number, which was analyzed over a fewer number of runs. The final aerothermal bulk properties of the test gas are a function of the measured shock speeds (primary and secondary) and the initial fill conditions (composition, pressure, and temperature). Properties labeled as "semitheoretical" were computed based on these parameters using the expansion tube solver. On the other hand, properties labeled as "measured" were acquired directly through the use of fast-response pressure sensors. Finally, the method of characteristics and unsteady shock wave theory are used to compute the theoretical test time using knowledge of the initial fill parameters and lengths of each of the three sections.

The indicated uncertainties (presented as percentages of the corresponding mean value) are defined based on the standard deviation between runs. Thus, they represent a shot-to-shot variation and not spatial and/or temporal uncertainty in the measurement method used because their contribution to the overall uncertainty budget was found to be inconsequential. For "measured" aerothermal properties (Mach number and static pressure) in region ⑤ of Fig. 1, the reported uncertainties are based on the temporal average and root-mean-square values computed over the useful test time.

The static pressure measured through the tube wall corresponds to a combined temporal average over the four shock counters in the expansion section. The average is over a period of time just after the passage of the secondary shock until a time in which the flow remains unaffected by the effects of boundary-layer growth. An example of this is shown in region ⑳ of Fig. 7. This is an indirect measure of the test gas pressure under ideal inviscid conditions, because it relies on the validity of the assumption of continuity in pressure imposed by the necessary kinematic constraints between regions ⑳ and ⑤. The static pressure measured in the test section is a temporal average of the test gas in region ⑤ over the useful test time indicated by region V in Fig. 7. The static pressure measured in the test section of region ⑤ is always greater than what is measured at the tube wall as a result of boundary-layer growth. Nevertheless, the "semitheoretical" value of static pressure agrees very well with the pressure measured at the tube wall just after the passage of the shock waves. This shows that the expansion tube solver is able to accurately compute the gas pressure when viscous effects are neglected.

The measured property "total test time" in Table 1 refers to the time between the arrival of the test gas (III) and the arrival of any of the rarefaction waves (VI) labeled in Fig. 6a. This is the ideal length of the test time if the contact surface were truly discontinuous and if viscous effects were negligible. On the other hand, the measured property "useful test time" refers to region V and corresponds to the region of the flow in which the pitot trace remains to within ±5% of its average value.

There are a number of conclusions that can be drawn from the information provided in Table 1. First, the shot-to-shot variability in the measured shock speeds is only a fraction of a percent. This is a result of repeatable initial filling of each section with the desired composition and pressure before each run; the close control over the initiation of the run; and the clean rupturing of the diaphragms that minimizes flow disturbances. The consequences of the shot-to-shot variability in the measured shock speeds on the final bulk test gas properties are shown by the properties labeled "semitheoretical" because their values depend on the measured shock speeds. Second, the measured properties such as Mach number compare well with their corresponding semitheoretical properties. Although the measured values of pressure used to infer the test gas Mach number in region V are greater than the ideal inviscid values, the Mach number during V compares well with the semitheoretical calculation.

C. Temporal Evolution of Bulk Flow Mach Number from Schlieren Imaging

To visually evaluate the temporal evolution of the flow, a standard Z-type schlieren system was set up to acquire kHz-rate schlieren images of the generated flow field as it developed over a 20° wedge. The high-speed images were captured with a Phantom v771 CMOS camera at a frame rate of 24 kHz and an exposure of 2 μs. Each image had a resolution of 256×152 pixels while the field of view was approximately 7.0 cm in the streamwise direction and 5.0 cm in the vertical direction. Continuous illumination was provided by an LED (Luminus SBR-70), which was collimated through the test section with a combination of lenses and spherical mirrors. The knife-edge was oriented horizontally to visualize density gradients in the vertical direction. Static pressure measurements downstream of the oblique shock were simultaneously acquired through a recessed-mounted fast-response piezoelectric pressure transducer instrumented inside the wedge. The captured images were reduced by removing dark noise and normalizing by the mean illumination field with no flow.

An example of two processed images extracted from the schlieren movie at different instances during the evolution of the flow is shown in Fig. 9. The pair of images, which pertain to flow condition B, is overlaid by a schematic of the wedge including the position of an internally mounted static pressure sensor. The first image in Fig. 9a shows the flow field during the passage of the contact surface (IV). The supersonic flow is just beginning to flow over the wedge and form a shock wave. Some diaphragm debris are also visible in this particular case. The second image in Fig. 9b shows the flowfield as the supersonic test gas flows over the wedge during the useful test time (V).

From each schlieren image composing the movie for a run, a spatially averaged Mach number of the flow upstream of the oblique shock was computed by measuring the wave angle and using the solution for oblique shock waves (for constant γ) [50]. A value of γ equal to the average between the values across the oblique shock was used. Figure 10a shows a time history of the inferred flow Mach number upstream of the oblique shock (M_5) for flow condition B. The vertical and horizontal error bars correspond to uncertainties in measuring the oblique shock angle and temporally correlating the images to the pressure trace, respectively. The results show a region

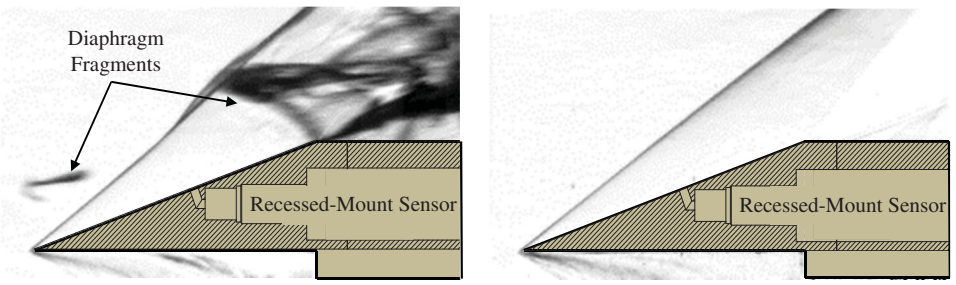

Fig. 9 Instantaneous snapshots of the flow structure around a 20° wedge during a) passage of the contact surface (IV) and b) useful test time (V). Data refer to flow condition B.

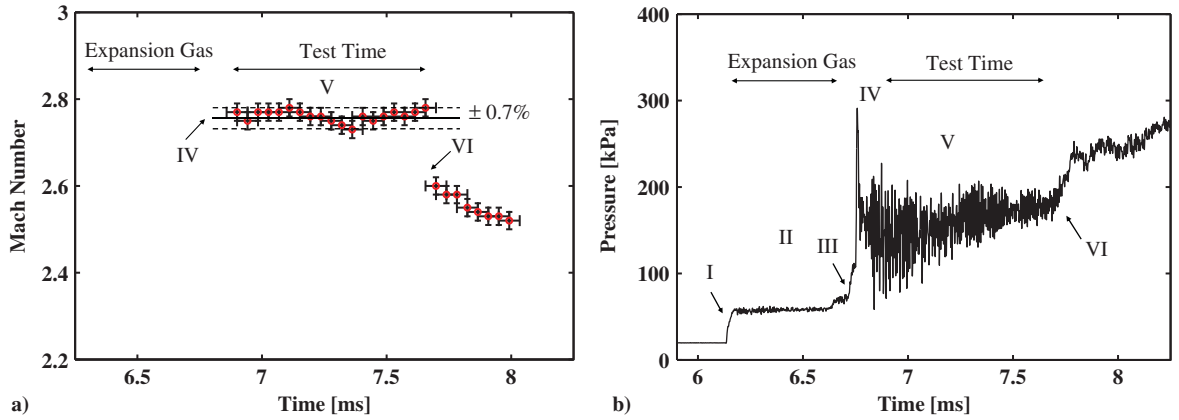

Fig. 10 a) Inferred gas Mach number based on measured oblique shock angle. b) Static pressure measured on wedge surface. Data pertain to condition B.

of uniform test gas flow where the standard deviation of the Mach number during the useful test time (V) is 0.7% of the mean value. On average, the measured oblique shock angle during the useful test time was 38.9°, which corresponds to a value of $M_5 = 2.76$. The uncertainty in measuring the wave angle translates to ±1.5% of M_5. This measured value of M_5 agrees well with the computed semitheoretical value as well as the Mach number inferred from the simultaneously measured pitot–static pressure measurements.

Figure 10b shows the corresponding time history of the static pressure measured on the surface of the wedge downstream of the oblique shock; labels identify the main phases of the flow evolution described previously. The measured time-average static pressure on the surface of the wedge during the useful test time was 165 kPa, which corresponds to a preshocked static pressure of 50 kPa. This value is 2% larger than the measured value using the pitot–static probe assembly. Based on this method, the inferred test gas Mach number for flow condition A was measured to be 1.96. This value is 4.3% less than the computed semitheoretical value of 2.05. The measured time-averaged static pressure during the useful test time was 317 kPa, which corresponds to a preshock static pressure of 118 kPa. This value is 3.5% lower than the measured value using the pitot–static probe assembly. This method was not used to measure the test gas Mach number for condition C because the lower test gas Mach number results in a detached oblique shock wave. Based on the limited cases considered here, it appears that this approach might tend to consistently underestimate the measured value of flow Mach number compared with the pitot–static assembly.

The experimental methods used in this study to indirectly measure or infer test gas properties have also been used in other facilities. Strand and Hanson [48,51] took measurements of flow properties in expansion tube flows, such as flow temperature and speed, using both direct and indirect methods similar to those used here. They found good agreement between the two methods, thus demonstrating that the type of measurements used in this study is capable of accurately capturing the bulk properties of the generated flows.

D. Evaluation of the Flow Spatial Uniformity

Because the test gas must travel several tube diameters before it reaches the test section, the growth of the boundary layer has a significant effect on the radial uniformity of the flow properties and the size of the core flow. Therefore, it is important to evaluate the effective core size of the flow and how test gas properties vary along the radial direction of the flow during the useful test time.

Radial distribution of properties was obtained by using a pitot rake assembly fixed in the test section approximately 3 mm from tube exit plane to ensure that the sensors were always within the test gas core flow. The rake was originally designed by Orley [52] to measure a total of 25 evenly distributed positions spanning the diameter of the tube ($2R = 144$ mm). This was done by instrumenting the rake with 5 pitot tubes evenly spaced 28.8 mm apart. The rake was then traversed across 5 evenly spaced positions 5.8 mm apart. The pitot tube design and instrumentation was identical to what was used in the pitot–static assembly. Unfortunately, due to calibration issues with one of the sensors, a portion of the data is omitted from the present work, and therefore the pitot pressure profiles consist of only 20 measurement points. A minimum of two experiments were carried out for each of the five pitot rake positions.

For each experimental run, pitot pressure measurements were temporally averaged over the useful test time to construct radial profiles of mean quantities. Typical time history measurements taken simultaneously at four radial locations across the diameter of the tube for condition A are shown in Fig. 11a. P_a is the mean static pressure over the useful test time and has a value of 122.4 kPa. The Roman numerals correspond to the description outlined in the previous section. The pitot measurements taken at positions $r/R = 0$ and ±0.4 are shown to lie within the core flow. These three traces have the

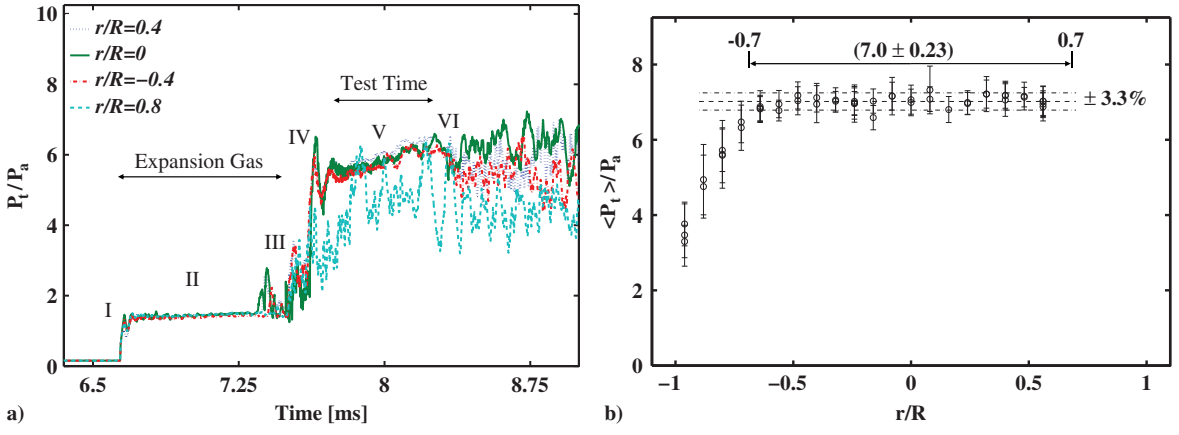

Fig. 11 a) Time history of pitot pressure measurements at four radial locations. b) Temporally averaged radial pitot profile. Data pertain to condition A.

same average value over the test time, and they also qualitatively have the same temporal evolution, including the small time-scale variations of pitot pressure observed during the evolution. More specifically, the cross-correlation coefficients computed from the pitot pressure traces within the core flow have a value very close to unity. These observations indicate that the core flow has some degree of radial homogeneity and that whatever feature causes the small time-scale variations is fairly planar. On the other hand, the pitot probe located at $r/R = 0.8$ exemplifies a trace of the pitot pressure at a point that is in the boundary layer of the flow. Within the boundary layer the value of the mean pitot pressure is lower than in the core (lower Mach number), the magnitude of the temporal fluctuations are larger, and the temporal evolution is poorly correlated to those measured within the core.

The radial profile of the temporally averaged pitot pressures for condition A is shown in Fig. 11b. The x axis of the figure is normalized by the inner radius of the tube, and the y axis was normalized by an average measured static pressure value of $P_a = 122.4$ kPa (see Table 1). The error bars correspond to the temporal standard deviation measured over the useful test time. From these measurements we can now quantify the size of the useful core flow, which is defined as the region where the value of the pitot pressure is within an acceptable range about the mean value. For case A, the useful core flow was found to span 70% of the inner diameter of the tube. The standard deviation of the temporally averaged values (circular symbols) in the useful core region was found to be within $\pm 3.3\%$ of their mean value, which is equal to $7.0P_a$. A similar procedure was followed for flow conditions B and C, and the resulting mean radial profiles (during the useful test time) are shown in Fig. 12. The results show that for all three cases, the flow properties across the tube diameter remain to within $\pm 5\%$ of the mean value in the useful core flow, which spans approximately $2/3$ of the tube diameter. There is, however, a small variation of the effective useful core size among the cases; the useful core size increases with increasing test gas pressure and was not found to correlate with Reynolds number.

E. Boundary-Layer Profile

The acquired pitot profile data were used to further characterize the test gas boundary layer. The computed flow Reynolds number, based on the bulk freestream properties and tube diameter, for each condition is tabulated in Table 1 for reference. Based on the work of [53], the transitional Reynolds number depends on the ratio of the wall-to-freestream temperatures, Mach number of the flow relative to the wall, and the ratio of the shock speed and the freestream speed in the shock-fixed coordinates. The transition Reynolds number was found to range between values of 5×10^5 and 5×10^7, which encompasses the Reynolds number values of this study. Therefore, the test gas boundary layers in this study are assumed to be turbulent.

By assuming that the static pressure is constant along the radial direction, approximate radial distributions of the temperature $T(r)$ and flow speed $U(r)$ were computed from the measured pitot pressure assuming that temperature and flow speed are related by the Crocco–Busemann relation (assuming unity Prandtl number):

$$T(r) = T_w + (T_{\text{aw}} - T_w)\frac{U(r)}{U_5} - \frac{1}{2}\frac{(\gamma - 1)}{\gamma}\frac{U(r)^2}{\mathcal{R}} \tag{9}$$

where the local speed is computed from the local Mach number $M(r)$ given from the measured pitot pressure using the Rayleigh pitot formula as:

$$U(r) = M(r)\sqrt{\gamma \mathcal{R} T(r)} \tag{10}$$

Here r is the radial distance from the centerline of the tube; T_w and T_{aw} are the wall and adiabatic wall temperatures, respectively; and U_5 and $\mathcal{R}$ are the test gas freestream speed and gas constant [50,54]. Owing to the short duration of the experiments, the wall temperature was taken to be room temperature. In addition, the estimated radial profile of the flow speed was then fit to an approximation profile. Assuming that the boundary layers are turbulent, a 1/7th power law approximation was used [54]:

$$\frac{U(r)}{U_5} = \begin{cases} 1, & r < R - \delta, \\ \left(\dfrac{R - r}{\delta}\right)^{1/7}, & r > R - \delta \end{cases} \tag{11}$$

where δ is the boundary-layer thickness corresponding to $U/U_5 = 0.99$ and it was found by a least-squares fitting of the measured radial profile to Eq. (11).

Figure 13a shows the resulting normalized radial profile of flow speed as a function of distance from the wall for the three cases. The distances from the wall for each condition are normalized by the corresponding boundary-layer thickness δi (i = A, B, and C). The 1/7th power law is also plotted and can be seen to describe the speed profiles quite well. The resulting average boundary-layer thicknesses $\delta i/R$ over the test time for conditions A, B, and C are 0.46, 0.43, and 0.51, respectively. The estimated thicknesses were not found to scale with the flow Reynolds number. The results of this procedure give a more conservative estimate of the useful core flow size as compared with the method defined in the previous section. Nevertheless, the two methods are in acceptable agreement.

This method is also used to evaluate the radial distribution of other quantities of interest defining the test gas properties. Figure 13b shows the corresponding radial profiles of temperature for each of the cases. The temperature profile for condition A has a monotonic behavior from the freestream through the boundary layer. On the other hand, the boundary-layer temperature for condition B increases past the freestream value because of the relatively larger freestream speed of the flow. The same nonmonotonic behavior is observed for condition C, where this time the relatively lower specific heat of the Argon test gas allows the transfer of energy to more readily increase the gas temperature within the boundary layer.

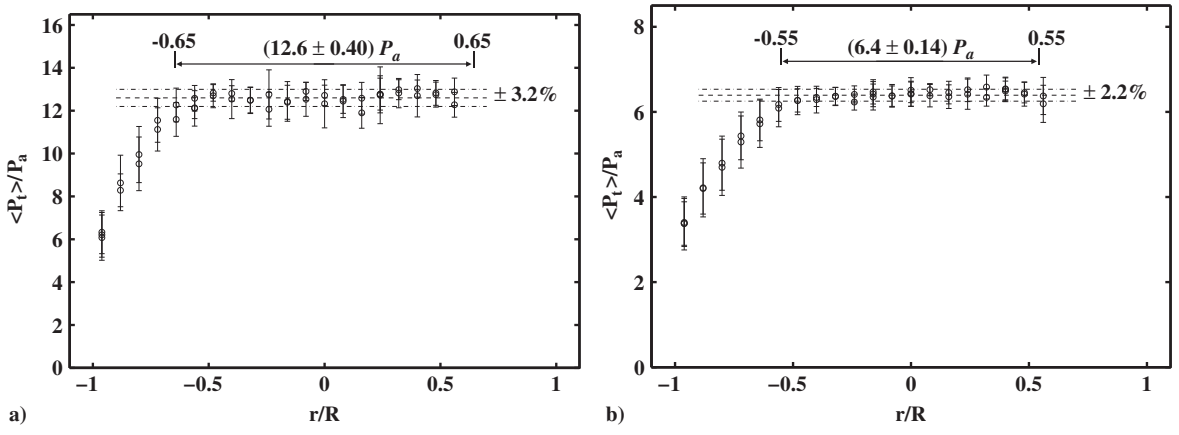

Fig. 12 Temporally averaged radial pitot profiles for conditions a) B and b) C.

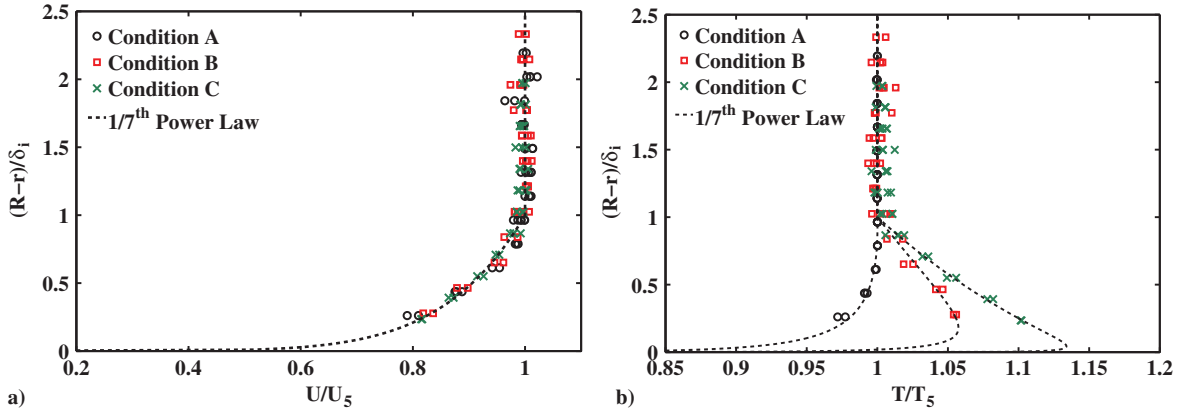

Fig. 13 a) Radial profiles of test gas speed compared with the 1/7th power law approximation. b) Radial profiles of test gas temperature.

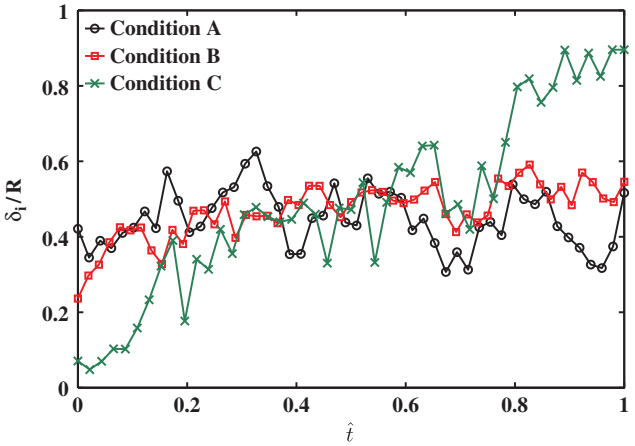

Fig. 14 Boundary-layer thickness as a function of time during the test gas flow.

It is also of interest to gain insight regarding the temporal evolution of the boundary layer. The useful test time was divided into segments of duration Δt and the boundary-layer thickness was extracted using the procedure described above from the average pitot pressure over the time segment. Δt was taken to be $1/50$ of the total useful test time. In this manner, the boundary-layer thickness for each condition δ_i was computed as a function of time. The results are illustrated in Fig. 14, where $\hat{t}$ is the time elapsed from the start of the test time normalized by the total useful test time for each respective flow condition.

It is difficult to discern a boundary-layer growth rate for condition A. This is a consequence of the relatively short test time, which is approximately $1/9$ of that of condition C. On the other hand, the results for conditions B and C reveal the behavior of the boundary layer as it grows over the test gas slug. It can also be seen that by the end of the test time, the flow for condition C has almost reached a state that is of a fully developed pipe flow (i.e., $\delta_C \to R$).

F. Flow Disturbances

A potential inherent limitation of expansion tube facilities is the presence of flow disturbances, which are observed in the form of significant pressure fluctuations in the final test gas, and limit the range of accessible conditions to only those with an acceptably steady test flow. The work of Paull and Stalker [22] showed that disturbances could be sufficiently modeled as first-order lateral acoustic waves. They postulated that the flow disturbances originate in the driver gas as a result of the primary diaphragm rupturing process. They define two limits in which an expansion tube facility may be operated: the high-enthalpy and low-enthalpy condition limits. The former is defined as when the sound speed of the shocked test gas is greater than that of the expanded driver gas, $a_2/a_3 > 1$, whereas the latter is when the facility is operated such that $a_2/a_3 < 1$.

There are two effects that one should consider regarding flow disturbances due to lateral waves. The first one is the extent in which disturbances are transmitted across an interface. In the case of a high-enthalpy condition, noise transmission through the contact surface is attenuated by increasing the ratio of a_2/a_3. The degree this ratio must be greater than unity reduces as a_3 increases because the contact surface behaves as a low-frequency filter, where the extent of noise filtering/attenuation increases with the ratio a_2/a_3 and a_3.

The second effect is the focusing of the range of frequencies of noise transmitted into the test gas. Frequency focusing occurs as the test gas is processed by the secondary unsteady expansion wave. This results in a final test gas flow with a noticeable narrow bandwidth noise, which can cause the test gas flow to be of limited use. Frequency focusing is mostly a concern when operating in the low-enthalpy regime, because noise will have more readily been transmitted into the test gas upon rupturing the primary diaphragm. They will then focus to unacceptable levels after being processed by the secondary expansion wave. In the laboratory reference frame, the dominant frequency in which noise is focused to across the secondary expansion wave is given by

$$\nu = \frac{\lambda(a_2 + ((\gamma_2 - 1)/2)U_2)}{2\pi[1 - ((\gamma_2 - 1)/2)^2]^{1/2}} \tag{12}$$

where γ_2 and U_2 are the ratio of specific heats and flow speed in region ②, and λ is the set of permissible values given by the infinite number of solutions of $J_1(\lambda R) = 0$, except for $\lambda R = 0$; J_1 is the first-order Bessel function of the first kind and R is the inner radius of the tube.

For the flow conditions used in this study, the values of a_2/a_3 were 1.0, 1.1, and 1.9, for flow conditions A, B, and C, respectively. These three conditions lie within the high-enthalpy regime of the expansion tube operating limits, using the definition described earlier. Therefore, one would expect a limited amount of noise transmitted into the test gas, and a negligible amount of focusing of the noise after being processed by the secondary expansion wave. The resulting focus frequencies [using Eq. (12)] for conditions A, B, and C are 7.1, 7.3, and 5.6 kHz, respectively. Figure 15 shows a spectral decomposition of the test gas for all three conditions. Moreover, the magnitude of disturbances with frequencies greater than 20 kHz is less than a value of 0.1 for all cases, indicating that greater pressure fluctuations are confined within a band in the lower frequency range. Although the conclusions are limited by the achievable spectral resolution, the calculated focus frequencies are not clearly apparent for any of the cases. Rather than a distinct frequency being amplified, a band of frequencies with relatively larger amplitudes is observed. However, the magnitudes are not sufficient enough to cause disturbances, which renders the test gas to be of no use. This is because the sound speed ratio across the secondary expansion a_5/a_2 was never lower than a value of 0.78 for any of the three conditions, resulting in a weak focusing effect. This is a similar observation to the one made in [23].

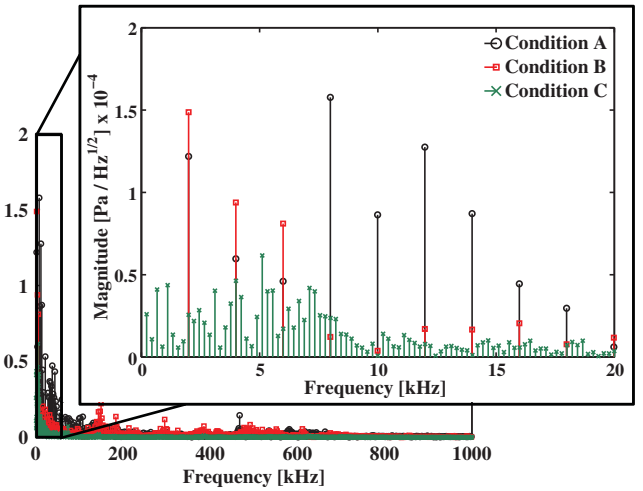

Fig. 15 Spectral decomposition of test gas pitot pressure traces for three flow conditions.

V. Improvements in Pressure Measurement Capabilities

The use of fast-response piezoelectric pressure sensors is a favored method for dynamic pressure measurements with impulse facilities such as expansion tubes [5,14,30,55–57]. This is because of their ability to survive in harsh environments and to respond within microseconds to step changes in pressure, while providing measurements with high signal-to-noise ratios (SNR). However, a series of experiments using the simultaneous pitot–static pressure measurement assembly, shown schematically in its original form by the inset of Fig. 6a and in the modified form in Fig. 16a, revealed a shortcoming in the ability of the sensor to accurately measure static pressure in such environments. Upon arrival of the test gas, the voltage output from the sensor is overwhelmed by high-amplitude noise that renders the pressure measurement useless. This effect has been observed in many situations in previous work with impulse facilities.

An example of a pressure signal with overwhelming amounts of noise is shown by the gray trace in Fig. 16b. This pressure trace was taken for flow condition B, and is a typical example of any static pressure trace acquired with the original mounting configuration of the sensor. This configuration consisted of flush-mounting the sensor, in a manner specified by the manufacturer, directly into the aluminum plate. Upon arrival of the test gas (III), the signal clearly failed to provide usable data as the pressure trace registered a negative value of pressure, and a standard deviation of $P_{\text{std}} = 56$ kPa.

The cause of the deficient pressure measurements was thought to be the vibrations in the assembly, which cause high-frequency oscillations. The arrival of the test gas results in a larger stagnation pressure experienced by the assembly and can be approximated as an impulsive force. This may be an issue because these sensors are not designed to compensate for lateral force loading on the sensing element; rather, they are designed to measure only axial forces. Also, due to the nature of such facilities, the time required for the system to dampen out such vibrations may very well exceed the test times.

The first attempt to reduce the noise in the pressure measurements was to test different PCB sensor models with varying sensitivities (ranging between 14.5 and 1.45 mV/kPa) in hopes of finding a model that was less susceptible to noise. After a series of experiments using three different sensors, it was concluded that no improvement in the SNR was made because the acquired signal standard deviations normalized by the mean pressures, $P_{\text{std}}/P_{\text{mean}}$, ranged between 0.2 and 1.5 regardless of which sensor was used. The results were in agreement with the fact that the PCB sensors tested only differed in the electrical components used to amplify the output, and did not differ in the mechanical stiffness of the sensing element or casing that may have dampened the vibrations by a varying extent.

The second attempt was to design an alternative method of mounting the static sensor and extends the work of [30]. The modified design is shown schematically in Fig. 16a. With this configuration, the static sensor is flush-mounted into a delrin sleeve with a diameter approximately equal to 3 sensor body diameters, in a manner specified by the manufacturer. The aluminum plate was bored with a diameter 2 mm larger than that of the delrin sleeve. The sleeve was flush-mounted into the plate while high-temperature RTV silicone was used to fill the space between the parts. The motivation behind this design was to provide a way for the subassembly holding the sensor to dampen the vibrations induced by the strong pressure waves resulting from the arrival of the test gas, while electrically insulating it from the rest of the assembly. Thus, the combination of delrin and RTV silicone was chosen to independently and collectively dissipate the mechanical energy in the form of vibrations by acting as a viscoelastic dampener. Delrin is also easily machinable. In addition, the pressure sensor was electrically grounded by attaching a ground strap from the sensor to the inside wall of the test section. This provided a pathway for charge buildup to move from the sensor, instead of contaminating the charge produced by the sensor going to the signal conditioner.

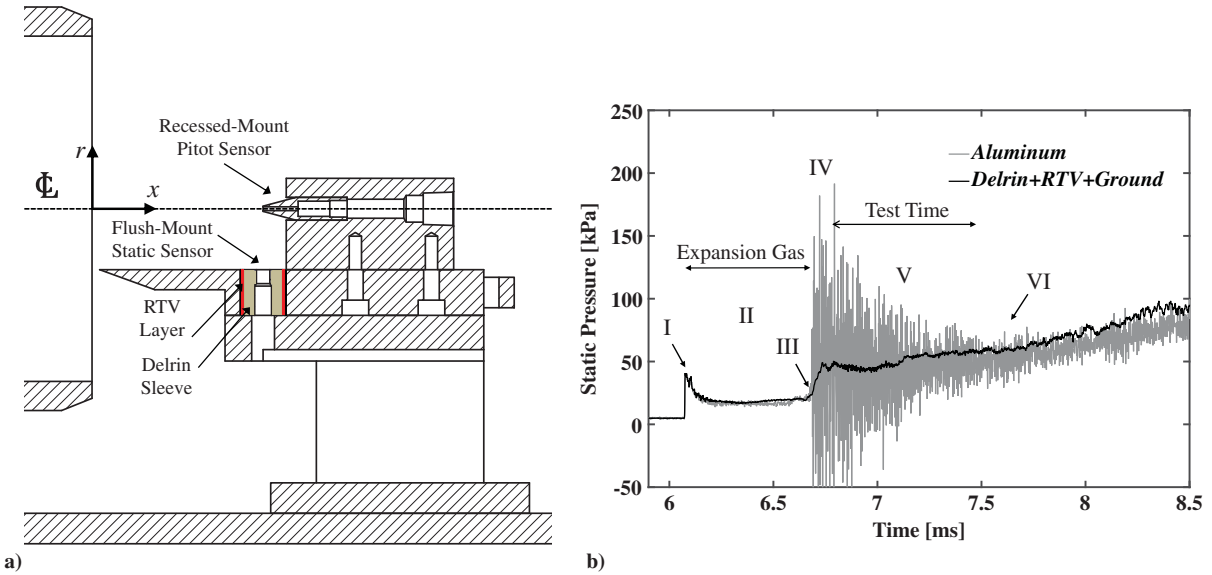

Fig. 16 a) Schematic of assembly with modified static sensor mounting. b) Flow condition B pressure measurements taken with and without the modified sensor mounting configuration.

An example of the static pressure trace with the modified configuration is shown by the green line in Fig. 16b. As a result of this alternative mounting strategy, there is a significant improvement in the quality of the measured pressure trace. A similar design approach was used for pressure measurement with the 20° wedge. The amount of noise, $P_{\text{std}}/P_{\text{mean}}$, was reduced by 70% and 50% for the pitot–static and wedge assemblies, respectively. The static pressure measurements reported in this work were all acquired with the modified sensor mounting configuration discussed in this section.

VI. Conclusions

This paper serves as the foundational groundwork for future supersonic mixing and combustion studies with the recently developed Michigan Hypersonic Expansion Tube Facility (MHExT). The MHExT facility is shown to be capable of generating a wide range of flows relevant to supersonic combustion studies with sufficiently long test times. Three flow conditions with relevance to supersonic mixing and combustion were designed and characterized in this study. The results provide insight regarding the characteristics of the generated flows as well as the extent in which expansion tube nonidealities affect the test gas properties. This paper has assessed the capability of the facility to repeatably generate the desired flows of interest, as well as the quality of the flows after being affected by nonideal effects such as boundary-layer growth and disturbances that result from diaphragm rupture.

A shot-to-shot statistical analysis of the measured shock speeds reveals a variability amounting to a fraction of a percent. The semitheoretical value of test gas static pressure agreed very well with the measured test gas pressure before being altered by viscous effects. The measured static pressure and total pressure of the test gas increased along the test gas slug. However, a useful test time, which was defined as the portion of the total test time over which the pitot pressure does not exceed ±5% of the mean value, was established for each condition.

The test gas Mach number was measured in two ways: 1) inferring it through simultaneously measured pitot and static pressures in the test section; 2) by measuring the oblique shock angle formed by a wedge using high-speed schlieren imaging. There was a good agreement between the semitheoretical and experimentally measured flow Mach number. Moreover, it was found that the increase in the measured pitot and static pressures over the test gas slug along with the nearly constant inferred Mach number implied that the total pressure of the test gas was increasing over the slug.

The test gas pressure was measured in several locations along the tube. There was a good agreement between the semitheoretical and experimentally measured test gas pressure before being affected by boundary-layer effects (state ⑳). However, the actual test gas flow pressure (state ⑤) was always systematically greater than the semitheoretical value for all three conditions as a result of boundary-layer effects.

Spatial pressure measurements with a pitot rake were used to characterize the core flow size and spatial uniformity of the test gas flow. A total of 20 radial locations along the expansion tube's exit plane were used to construct radial pressure profiles of the test gas flow. The useful core flow was found to vary between $r/R = 0.55$ and $r = 0.70$ among all three cases, where the core size was larger with higher values of test gas pressure. The temporal mean value of the core flow pressure during the useful test gas at each radial location was found to vary by less than ±3.3% of the mean core pressure for all three cases.

A spectral decomposition of the test gas pitot pressures was computed and compared with the work in [22]. The test gas conditions in the present study displayed minimal flow disturbances due to the regime in which they were operated. Finally, an improvement in the pressure measurement capabilities with such an impulse facility was discussed. The results showed a significant increase in signal-to-noise ratios by mounting the sensor in a delrin sleeve coated in high-temperature RTV, as well as grounding the signal cables.

Appendix: Expansion Tube Solvers

Two zero-dimensional expansion tube solvers are used in this study. The solvers are inviscid, equilibrium, temperature-dependent property models. The first solver requires experimentally measured shock speeds (primary and secondary), and initial fill conditions of each section (composition, temperature, and pressure) as inputs to solve for the thermodynamic properties of the various states of gas. The model solves for the jump conditions across the primary and secondary shock waves, and matches conditions across the secondary unsteady expansion wave assumed to be an isentropic centered expansion. The model follows a treatment (and nomenclature) similar to what was given by Trimpi [27]. The "semitheoretical" properties reported in this study were computed using this solver.

The model numerically solves for the Rankine–Hugoniot (R-H) jump conditions [50] across a moving shock wave using equilibrium, temperature-dependent properties. The properties are approximated using the NASA polynomial fits to the gas thermodynamic properties, such as the specific heats [58]. For the changes across a normal shock moving at a speed W and processing a gas at an initial state ① to a final state ②, the R-H conditions can be written as

$$\left(\frac{P_2 - P_1}{\rho_2 - \rho_1}\right) - \frac{\rho_1}{\rho_2} W^2 = 0 \tag{A1}$$

$$(h_2 - h_1) - \frac{P_2 - P_1}{2}\left(\frac{1}{\rho_1} - \frac{1}{\rho_2}\right) = 0 \tag{A2}$$

Along with the equation of state $h = \tilde{h}(T)$ given by the NASA polynomial fits [58], Eqs. (A1) and (A2) are two equations where the two unknowns, P_2 and T_2, are numerically solved using a least-squares minimization scheme. This solution is implemented for both the primary and secondary shock waves.

The secondary expansion wave is modeled using the method of characteristics for one-dimensional, unsteady, isentropic wave propagation, imposing that pressure and speed across the secondary contact surface are constant. Because the solution of the secondary shock wave (from the measured shock speed) effectively gives the values of P_5 and U_5, the model reduces to solving the isentropic condition $s_2 - s_5 = 0$ for the final temperature T_5 using an equilibrium, temperature-dependent expression for entropy ($s = \tilde{s}(T, P)$) derived from the NASA polynomial fits [58]. The solution is found numerically using a least-squares minimization method.

The second solver is used to design test gas conditions without any knowledge or measurement of the shock speeds. It only requires the initial fill conditions of each section. In this case, the compatibility equation

$$du + \frac{dh}{a} = 0 \tag{A3}$$

is integrated across the expansion wave to solve for the additional unknown variable.

References

[1] Jackson, K. R., Gruber, M. R., and Buccellato, S., "Mach 6–8+ Hydrocarbon-Fueled Scramjet Flight Experiment: The HIFiRE Flight 2 Project," *Journal of Propulsion and Power*, Vol. 31, No. 1, 2015, pp. 36–53. doi:10.2514/1.B35350

[2] Smart, M. K., Hass, N. E., and Paull, A., "Flight Data Analysis of the HyShot 2 Scramjet Flight Experiment," *AIAA Journal*, Vol. 44, No. 10, Oct. 2006, pp. 2366–2375. doi:10.2514/1.20661

[3] Jackson, K., Gruber, M., and Buccellato, S., "HIFiRE Flight 2 Overview and Status Update 2011," AIAA Paper 2011-2202, 2011. doi:10.2514/6.2011-2202

[4] Laurence, S., Schramm, J. M., Karl, S., and Hannemann, K., "An Experimental Investigation of Steady and Unsteady Combustion

Phenomena in the Hysgot II Combustor," AIAA Paper 2011-2310, 2011, doi:10.2514/6.2011-2310

[5] Lu, F., and Dan, M., *Advanced Hypersonic Test Facilities*, AIAA, Reston, VA, 2002. doi:10.2514/4.866678

[6] Lukasiewicz, J., *Experimental Methods of Hypersonics*, Marcel Dekker, New York, 1973. doi:10.1017/s0022112074211923

[7] Dufrene, A., Maclean, M., and Wadhams, T., "Characterization of the New LENS Expansion Tunnel Facility," AIAA Paper 2010-1564, 2010. doi:10.2514/6.2010-1564

[8] Calleja, J., and Tamagno, J., "Calibration of HYPULSE for Hypervelocity Mach Air Flows Corresponding to Flight Numbers 13.5, 15, and 17," NASA Contractor Rept. 191578, 1993.

[9] John, I., Bakos, R. J., Castrogiovanni, A., Rogers, R. C., and Rogers, R. C., "Dual Mode Shock-Expansion/Reflected-Shock Tunnel," AIAA Paper 1997-0560, 1997. doi:10.2514/5.9781600866678.0029.0071

[10] Paull, A., and Stalker, R., "Scramjet Testing in the T3 and T4 Hypersonic Impulse Facilities," *Scramjet Propulsion*, AIAA, Reston, VA, 2000, Chap. 1, pp. 1–46.

[11] Neely, A., and Morgan, R., "The Superorbital Expansion Tube Concept, Experiment and Analysis," *The Aeronatutical Journal*, Vol. 98, No. 973, 1994, pp. 97–105. doi:10.1017/S0001924000050107

[12] Stalker, R., Paull, A., Mee, D. J., Morgan, R. G., and Jacobs, P., "Scramjets and Shock Tunnels—The Queensland Experience," *Progress in Aerospace Sciences*, Vol. 41, No. 6, 2005, pp. 471–513. doi:10.1016/j.paerosci.2005.08.002

[13] Hornung, H., Sturtvant, B., Bélanger, J., Sanderson, S., Brouillette, M., and Jenkins, M., "Performance Data of the New Free-Piston Shock Tunnel T5 at GALCIT," *Shock Waves: Proceedings of the 18th International Symposium on Shock Waves*, edited by K. Takayama, Springer, Berlin, 1992, pp. 603–610. doi:10.1007/978-3-642-77648-9_95

[14] Dufrene, A., Sharma, M., and Austin, J. M., "Design and Characterization of a Hypervelocity Expansion Tube Facility," *Journal of Propulsion and Power*, Vol. 23, No. 6, Nov. 2007, pp. 1185–1193. doi:10.2514/1.30349

[15] Sasoh, A., Ohnishi, Y., Koremoto, K., and Takayama, K., "Operation Design and Performance of a Free-Piston-Driven Expansion Tube," *37th Aerospace Sciences Meeting and Exhibit*, AIAA Paper 1999-825, 1999. doi:10.2514/6.1999-825

[16] Itoh, K., Ueda, S., Komuro, T., Sato, K., Takahashi, M., Miyajima, H., Tanno, H., and Muramoto, H., "Improvement of a Free Piston Driver for a High-Enthalpy Shock Tunnel," *Shock Waves*, Vol. 8, No. 4, 1998, pp. 215–233. doi:10.1007/s001930050115

[17] Itoh, K., Ueda, S., Komuro, T., Sato, K., Tanno, H., and Takahashi, M., "Hypersonic Aerothermodynamic and Scramjet Research Using High Enthalpy Shock Tunnel," *Shock Waves*, Vol. 12, No. 2, 2002, pp. 93–98. doi:10.1007/s00193-002-0147-0

[18] Beck, W., Eitelberg, G., McIntyre, T., Baird, J., Lacey, J., and Simon, H., "The High Enthalpy Shock Tunnel in Göttingen (HEG)," *Shock Waves: Proceedings of the 18th International Symposium on Shock Waves*, edited by K. Takayama, Springer, Berlin, 1992, pp. 677–682. doi:10.1007/978-3-642-77648-9_106

[19] Hannemann, K., Karl, S., Schramm, J. M., and Steelant, J., "Methodology of a Combined Ground Based Testing and Numerical Modelling Analysis of Supersonic Combustion Flow Paths," *Shock Waves*, Vol. 20, No. 5, 2010, pp. 353–366. doi:10.1007/s00193-010-0269-8

[20] Mirels, H., "Shock Tube Test Time Limitation Due to Turbulent-Wall Boundary Layer," *AIAA Journal*, Vol. 2, No. 1, 1964, pp. 84–93. doi:10.2514/3.2218

[21] Mirels, H., "Flow Nonuniformity in Shock Tubes Operating at Maximum Test Times," *Physics of Fluids*, Vol. 9, No. 10, 1966, pp. 1907–1912. doi:10.1063/1.1761542

[22] Paull, A., and Stalker, R., "Test Flow Disturbances in an Expansion Tube," *Journal of Fluid Mechanics*, Vol. 245, Dec. 1992, pp. 493–521. doi:10.1017/S0022112092000569

[23] Paull, A., and Stalker, R. J., "The Effect on an Acoustic Wave as It Traverses an Unsteady Expansion," *Physics of Fluids*, Vol. 3, No. 4, 1991, pp. 717. doi:10.1063/1.858079

[24] Malo-Molina, F. J., Gaitonde, D. V., Ebrahimi, H. B., and Ruffin, S. M., "Three-Dimensional Analysis of a Supersonic Combustor Coupled to Innovative Inward-Turning Inlets," *AIAA Journal*, Vol. 48, No. 3, 2010, pp. 572–582. doi:10.2514/1.43646

[25] Bricalli, M. G., Brown, L. M., and Boyce, R. R., "Supersonic Combustion Processes in a Premixed Three-Dimensional Nonuniform-Compression Scramjet Engine," *AIAA Journal*, Vol. 52, No. 8, 2014, pp. 1670–1685. doi:10.2514/1.J052640

[26] Gruber, M. R., Hagenmaier, M. A., and Mathur, T., "Simulating Inlet Distortion Effects in a Direct-Connect Scramjet Combustor," *42nd AIAA/ASME/SAE/ASEE Joint Propulsion Conference & Exhibit*, AIAA Paper 2006-4680, 2006. doi:10.2514/6.2006-4680

[27] Trimpi, R., "Preliminary Theoretical Study of the Expansion Tube, a New Device for Producing High Enthalpy Short Duration Hypersonic Gas Flows," NASA Technical Rept. 133, 1962. doi:10.1002/9781119113126.ch5

[28] Heiser, W. H., and Pratt, D. T., *Hypersonic Airbreathing Propulsion*, 6th ed., AIAA, Washington, D.C., 1994, Chap. 2. doi:10.2514/4.470356

[29] Luo, F., Song, W., Zhang, Z., Li, W., and Li, J., "Experimental and Numerical Studies of Vitiated Air Effects on Hydrogen-fueled Supersonic Combustor Performance," *Chinese Journal of Aeronautics*, Vol. 25, No. 2, April 2012, pp. 164–172. doi:10.1016/S1000-9361(11)60375-0

[30] Miller, V. A., Gamba, M., Mungal, M. G., and Hanson, R. K., "Secondary Diaphragm Thickness Effects and Improved Pressure Measurements in an Expansion Tube," *AIAA Journal*, Vol. 52, No. 2, Feb. 2014, pp. 451–456. doi:10.2514/1.J052767

[31] Furukawa, T., Aochi, T., and Sasoh, A., "Expansion Tube Operation with Thin Secondary Diaphragm," *AIAA Journal*, Vol. 45, No. 1, Jan. 2007, pp. 214–217. doi:10.2514/1.23846

[32] Anderson, G., Kumar, A., and Erdos, J., "Progress in Hypersonic Combustion Technology with Computation and Experiment," AIAA Paper 1990-5254, 1990. doi:10.2514/6.1990-5254

[33] Pergament, H., "A Theoretical Analysis of Non-Equilibrium Hydrogen-Air Reactions in Flow Systems," AIAA Paper 1963-113, 1963. doi:10.2514/6.1963-113

[34] Wang, H., You, X., Joshi, A., Davis, S., Laskin, A., Egolfopoulos, F., and Law, C., "USC Mech Version II. High-Temperature Combustion Reaction Model of H2/CO/C1-C4 Compunds," May 2007, http://ignis.usc.edu/USC_Mech_II.htm [retrieved July 2016].

[35] Zhukov, V. P., Sechenov, V. A., and Starikovskiy, A. Y., "Autoignition of Kerosene (Jet-A)/Air Mixtures Behind Reflected Shock Waves," *Fuel*, Vol. 126, 2014, pp. 169–176. doi:10.1016/j.fuel.2014.02.036

[36] De Toni, A., Werler, M., Hartmann, R., Cancino, L., Schießl, R., Fikri, M., Schulz, C., Oliveira, A., Oliveira, E., and Rocha, M., "Ignition Delay Times of Jet A-1 Fuel: Measurements in a High-Pressure Shock Tube and a Rapid Compression Machine," *Proceedings of the Combustion Institute*, Vol. 36, No. 3, 2017, pp. 3695–3703. doi:10.1016/j.proci.2016.07.024

[37] Kumar, K., and Sung, C.-J., "An Experimental Study of the Autoignition Characteristics of Conventional Jet Fuel/Oxidizer Mixtures: Jet-A and JP-8," *Combustion and Flame*, Vol. 157, No. 4, April 2010, pp. 676–685. doi:10.1016/j.combustflame.2010.01.001

[38] Davies, W., and Bernstein, L., "Heat Transfer and Transition to Turbulence in the Shock-Induced Boundary Layer on a Semi-Infinite Flat Plate," *Journal of Fluid Mechanics*, Vol. 36, No. 1, 1969, pp. 87–112. doi:10.1017/S0022112069001534

[39] Holden, M. S., "Boundary-Layer Displacement and Leading-Edge Bluntness Effects on Attached and Separated Laminar Boundary Layers in a Compression Corner. Part II: Experimental Study," *AIAA Journal*, Vol. 9, No. 1, 1971, pp. 84–93. doi:10.2514/3.6127

[40] Holden, M. S., "Establishment Time of Laminar Separated Flows," *AIAA Journal*, Vol. 9, No. 11, 1971, pp. 2296–2298. doi:10.2514/3.6512

[41] Miles, J., Mirels, H., and Wang, H., "Time Required for Establishing Detached Bow Shock," *AIAA Journal*, Vol. 4, No. 6, 1966, pp. 1127–1128. doi:10.2514/3.3633

[42] Mallinson, S. G., Gai, S. L., and Mudford, N. R., "Establishment of Steady Separated Flow over a Compression-Corner in a Free-Piston

Shock Tunnel," *Shock Waves*, Vol. 7, No. 4, 1997, pp. 249–253. doi:10.1007/s001930050080

[43] Farris, M. H., and Russell, C. T., "Determining the Standoff Distance of the Bow Shock: Mach Number Dependence and Use of Models," *Journal of Geophysical Research*, Vol. 99, No. A9, 1994, pp. 17681–17689. doi:10.1029/94JA01020

[44] Gamba, M., and Mungal, M. G., "Ignition, Flame Structure and Near-Wall Burning in Transverse Hydrogen Jets in Supersonic Crossflow," *Journal of Fluid Mechanics*, Vol. 780, 2015, pp. 226–273. doi:10.1017/jfm.2015.454

[45] Crist, S., Sherman, P. M., and Glass, D. R., "Study of the Highly Underexpanded Sonic Jet," *AIAA Journal*, Vol. 4, No. 1, 1966, pp. 68–71. doi:10.2514/3.3386

[46] Ashkenas, H., and Sherman, F., "Structure and Utilization of Supersonic Free Jets in Low Density Wind Tunnels," NASA CR-60423, Vol. 222, No. 45, 1962.

[47] Andronov, V., "Turbulent Mixing at Contact Surface Accelerated by Shock Waves," *Journal of Experimental and Theoretical Physics*, Vol. 44, No. 2, 1977, pp. 424–427. doi:10.1063/1.1693046

[48] Strand, C. L., and Hanson, R. K., "Quantification of Supersonic Impulse Flow Conditions via High-Bandwidth Wavelength Modulation Absorption Spectroscopy," *AIAA Journal*, Vol. 53, No. 10, 2015, pp. 2978–2987. doi:10.2514/1.J053842

[49] Ben-Yakar, A., and Hanson, R. K., "Characterization of Expansion Tube Flows for Hypervelocity Combustion Studies," *Journal of Propulsion and Power*, Vol. 18, No. 4, 2002, pp. 943–952. doi:10.2514/2.6021

[50] Liepmann, H. W., and Roshko, A., *Elements of Gas Dynamics*, Dover Publ., New York, 1957, Chaps. 4, 12. doi:10.1093/acprof:oso/9780199552689.003.0010

[51] Orley, B. F., Strand, C. L., Miller, V. A., Gamba, M., Adams, N. A., and Iaccarino, G., "A Study of Expansion Tube Gas Flow Conditions for Scramjet Combustor Model Testing," AIAA Paper 2012-3264, *Annual Research Briefs*, Center for Turbulence Research, 2011, pp. 285–296. doi:10.2514/6.2012-3264

[52] Orley, F., "A Study of Expansion Tube Gas Flow Conditions for Scramjet Combustor Model Testing," Ph.D. Thesis, Technische Univ. Munchen, Munich, 2011.

[53] Hartunian, R., Russo, A., and Marrone, P., "Boundary-Layer Transition and Heat Transfer in Shock Tubes," *Journal of the Aerospace Sciences*, Vol. 27, No. 8, 1960, pp. 587–594. doi:10.2514/8.8656

[54] White, F., *Viscous Fluid Flow*, 2nd ed., McGraw–Hill, New York, 1991, Chap. 7.

[55] McGilvray, M., Austin, J. M., Sharma, M., Jacobs, P. A., and Morgan, R. G., "Diagnostic Modelling of an Expansion Tube Operating Condition," *Shock Waves*, Vol. 19, No. 1, Feb. 2009, pp. 59–66. doi:10.1007/s00193-009-0187-9

[56] McGilvray, M., Jacobs, P. A., Morgan, R. G., Gollan, R. J., and Jacobs, C. M., "Helmholtz Resonance of Pitot Pressure Measurements in Impulsive Hypersonic Test Facilities," AIAA Paper 2009-1157, 2009, doi:10.2514/1.42543

[57] Sutcliffe, M. A., and Morgan, R. G., "The Measurement of Pitot Pressure in High Enthalpy Expansion Tubes," *Measurement Science and Technology*, Vol. 12, No. 3, 2001, pp. 327–334. doi:10.1088/0957-0233/12/3/312

[58] McBridge, B., Gordon, S., and Reno, M., "Coefficients for Calculating Thermodynamic and Transport Properties of Individual Species," NASA TM-4513, 1993, doi:19940013151

R. D. W. Bowersox
Associate Editor